Accepted Manuscript

Structural evolution of the Irtysh Shear Zone (northwestern China) and implications for the amalgamation of arc systems in the Central Asian Orogenic Belt

Pengfei Li, Min Sun, Gideon Rosenbaum, Keda Cai, Yang Yu

PII: S0191-8141(15)30026-2

DOI: 10.1016/j.jsg.2015.08.008

Reference: SG 3258

To appear in: *Journal of Structural Geology*

Received Date: 21 May 2015

Revised Date: 15 August 2015

Accepted Date: 20 August 2015

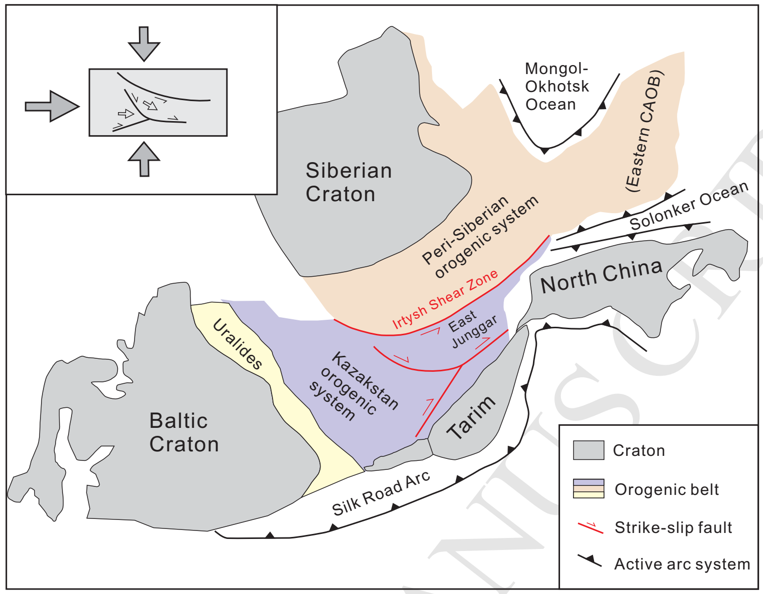

Siberian Craton
Mongol-Okhotsk Ocean
(Eastern CAOB)
Peri-Siberian orogenic system
Solonker Ocean
Irtysh Shear Zone
North China
East Junggar
Uralides
Kazakstan orogenic system
Baltic Craton
Tarim
Silk Road Arc
Craton
Orogenic belt
Strike-slip fault
Active arc system

Structural evolution of the Irtysh Shear Zone (northwestern China) and implications for the amalgamation of arc systems in the Central Asian Orogenic Belt

Pengfei Li [1], Min Sun [1], Gideon Rosenbaum [2], Keda Cai [3], Yang Yu [1]

[1] Department of Earth Sciences, The University of Hong Kong, Pokfulam Road, Hong Kong, China

[2] School of Earth Sciences, The University of Queensland, Brisbane 4072, Queensland, Australia

[3] Xinjiang Research Center for Mineral Resources, Xinjiang Institute of Ecology and Geography, Chinese Academy of Sciences, Urumqi 830011, China

*Corresponding author: Department of Earth Sciences, The University of Hong Kong, Pokfulam Road, Hong Kong, China. Email: pengfei@hku.hk; pengfeili2013@gmail.com

Abstract: The NW-SE Irtysh Shear Zone is a major tectonic boundary in the Central Asian Orogenic Belt (CAOB), which supposedly records the amalgamation history between the peri-Siberian orogenic system and the Kazakhstan/south Mongolia orogenic system. However, the tectonic evolution of the Irtysh Shear Zone is not fully understood. Here we present new structural and geochronological data, which together with other constraints on the timing of deformation suggests that the Irtysh Shear Zone was subjected to three phases of deformation in the late Paleozoic. D_1 is locally recognized as folded foliations in low strain areas and as an internal fabric within garnet porphyroblasts. D_2 is represented by a shallowly dipping fabric and related ~NW-SE stretching lineations oriented sub-parallel to the strike of the orogen. D_2 foliations are folded by ~NW-SE folds (F_3) that are bounded by zones of mylonitic foliations (S_3) with evidence for sinistral/reverse kinematics. These fold and shear structures are kinematically compatible, and thus interpreted to result from a transpressional deformation phase (D_3). Two samples of mica schists yielded youngest detrital zircon peaks at ~322 Ma, placing a maximum constraint on the timing of D_1-D_3 deformation. A ~NE-SW granitic dyke swarm (~252 Ma) crosscuts D_3 fold structures and mylonitic fabrics in the central part of the shear zone, but is displaced by a mylonite zone that represents the southern boundary of the Irtysh Shear Zone. This observation indicates that the major phase of D_3 transpressional deformation took place prior to ~252 Ma, although later phases of reactivation in the Mesozoic and Cenozoic are likely. The late Paleozoic deformation (D_1-D_3 at ~322-252 Ma)

overlaps in time with the collision between the Chinese Altai and the intra-oceanic arc system of the East Junggar. We therefore interpret that three episodes of late Paleozoic deformation represent orogenic thickening (D_1), collapse (D_2), and transpressional deformation (D_3) during the convergence between the Chinese Altai and the East Junggar. On a larger scale, late Paleozoic sinistral shearing (D_3), together with dextral shearing farther south, accommodated the eastward migration of internal segments of the western CAOB, possibly associated with the amalgamation of multiple arc systems and continental blocks during the late Paleozoic.

Key words: Central Asian Orogenic Belt; Irtysh Shear Zone; Chinese Altai; Junggar; Accretionary Orogen; Structural synthesis

1. Introduction

The Central Asian Orogenic Belt (CAOB) is the largest Phanerozoic orogenic collage in the world. It was subjected to a prolonged history of accretion from the late Mesoproterozoic to Mesozoic, following the closure of the Paleo-Asian Ocean (Zonenshain et al., 1990; Şengör et al., 1993; Khain et al., 2002; Xiao et al., 2003; Yakubchuk, 2004; Windley et al., 2007; Van der Voo et al., 2015; Xiao et al., 2015). Tectonic reconstructions of the CAOB are relatively poorly constrained, but it is generally agreed that orogenesis during the Paleozoic involved progressive accretion of continental and oceanic components along the convergent plate margins, followed by the collision and amalgamation of Siberian, Baltica, Tarim and North China cratons (Windley et al., 2007; Wilhem et al., 2012; Xiao and Santosh, 2014). This process has been accompanied by voluminous input of juvenile magma (Jahn et al., 2000; Jahn, 2004; Li et al., 2013; Kröner et al., 2014), oroclinal bending (Şengör et al., 1993; Van der Voo, 2004; Levashova et al., 2007; Lehmann et al., 2010; Xiao et al., 2010; Bazhenov et al., 2012), and the development of large scale strike-slip fault systems (e.g. Şengör and Natal'in, 1996).

One interesting characteristic of the CAOB is its vast width (>1000 km), which may have resulted from terrane accretion (Windley et al., 2007; Xiao and Santosh, 2014; Han et al., 2015), oroclinal bending (Van der Voo, 2004; Levashova et al., 2007; Lehmann et al., 2010; Xiao et al., 2010) and/or the lateral duplication of orogenic segments by strike-slip faulting (Laurent-Charvet et al., 2003; Buslov et al., 2004a). The role of strike-slip faults is important not only for understanding the orogenic width, but also for reconstructing the paleogeography of each orogenic segment that may have been displaced laterally. A large number of strike-slip faults and shear zones were developed in the Paleozoic (Allen et al., 1995; Laurent-Charvet et al., 2003; Buslov et al., 2004a; Alexeiev et al., 2009; Glorie et al., 2012b; Rolland et al., 2013), either in response to the amalgamation of arc systems or as a result of reactivation of inherited structures accommodating the relative movement of continental blocks in the Paleozoic (Allen et al., 2001; Xiao et al., 2009a; Glorie et al., 2011b; Han et al., 2011; Eizenhöfer et al., 2014). In the Mesozoic to Cenozoic, the western CAOB was subjected to intracontinental deformation, as constrained by low temperature thermochronolgical data (Dumitru et al., 2001; Jolivet et al., 2007; Vassallo et al., 2007; Jolivet et al., 2009; Jolivet et al., 2010; Glorie and De Grave, 2015). During this period, major Paleozoic faults and shear zones were reactivated (e.g. Glorie et al., 2011a; Glorie et al., 2011b; Glorie et al., 2012a; Glorie et al., 2012b).

The Irtysh Shear Zone (also known as Erqis, Irtishi, Ertix) or Irtysh Tectonic Belt, is one of the largest strike-slip shear zones in the CAOB (Fig. 1) (Şengör et al., 1993; Briggs et al., 2007). The surface-exposed shear zone extends >1000 km from NE Kazakhstan to NW China, and is connected to the Bulgan Fault in western Mongolia. The Irtysh Shear Zone represents the tectonic boundary between the peri-Siberian orogenic system and the Kazakhstan/south Mongolian orogenic system (Fig. 1) (Ren et al., 1980), which were separated from each other by the Ob-Zaisan Ocean (part of the Paleo-Asian Ocean), as recorded by ophiolites within the shear zone (Buslov et al., 2001; Wang et al., 2012 and reference therein). The exact active time of the Irtysh Shear Zone is not well constrained. $^{40}Ar/^{39}Ar$ thermochronological data along the Irtysh Shear Zone indicate that sinistral movements occurred at ~290-265 Ma in the

Kazakhstan segment (Buslov et al., 2004b, and references therein; Vladimirov et al., 2008), and at ~290-244 Ma in the Chinese segment (Laurent-Charvet et al., 2003; Briggs et al., 2007; Li et al., 2015b). Constraints on the timing of regional exhumation are available from apatite fission track data from the Kazakhstan segment of the Irtysh Shear Zone and the Chinese Altai to the north of the Irtysh Shear Zone, which yielded Cretaceous to Tertiary ages that are likely related to sinistral reactivation of the Irtysh Shear Zone (Yuan et al., 2006; Glorie et al., 2012b).

The Chinese segment of the Irtysh Shear Zone is well exposed in the Fuyun area (Figs. 1 and 2) in northern Xinjiang. This segment has been described as a crustal-scale fault system (Wang et al., 2003) that records the amalgamation between the Chinese Altai (part of peri-Siberian orogenic system) and the intraoceanic arc system of the West/East Junggar (part of the Kazakhstan/south Mongolian orogenic system) (Xiao et al., 2009b; Zhang et al., 2012). However, the deformation history of the Chinese segment of the Irtysh Shear Zone is controversial. It has been proposed that the shear zone accommodated sinistral shearing and a contractional component in response to oblique convergence between the Chinese Altai and the East/West Junggar (Qu, 1991; Qu and Zhang, 1991; Zhang and Zheng, 1993; Qu and Zhang, 1994; Laurent-Charvet et al., 2002; Laurent-Charvet et al., 2003). In contrast, Briggs et al. (2007; 2009) interpreted the so-called Irtysh Shear Zone to be a thrust belt, based on the local recognition of reverse faults. Structural fabrics that predated sinistral shearing were also reported within the shear zone (Qu and Zhang, 1991), but the origin and tectonic significance of such structures remain unclear due to insufficient structural and geochronological constraints.

We conducted structural analysis across the Chinese segment of the Irtysh Shear Zone with the aim of better understanding its deformational history and geodynamic significance. Our structural investigation was complemented by a geochronological study, which together with published chronological data (e.g. Briggs et al., 2007), allows us to link the deformation process with the tectonic evolution of the CAOB. Our results show that the Irtysh Shear Zone was subjected to three phases of late Paleozoic deformation (D_1-D_3), with the D_3 sinistral transpressional deformation likely associated with the late Paleozoic amalgamation of multiple arc systems and continental blocks. Our study mainly focuses on the late Paleozoic tectonic history of the Irtysh Shear Zone, with less emphasis on the role of Mesozoic and Cenozoic reactivation (e.g. Glorie et al., 2012b).

2. Geological setting

The Chinese Altai records the Paleozoic accretion history along the margin of the Siberian Craton (Windley et al., 2002; Safonova, 2013). In the latest Paleozoic, the Chinese Altai, as part of peri-Siberian orogenic system (Fig. 1a), was amalgamated with the Kazakhstan/south Mongolian orogenic system that is partly represented by the intra-oceanic arc system of the West/East Junggar (Fig. 1) (Windley et al., 2007; Xiao et al., 2008; Xiao et al., 2009b). The Irtysh Shear Zone is considered to represent the suture marking the amalgamation of these two orogenic systems (e.g. Xiao et al., 2015).

The Chinese Altai is characterized by a series of fault-bounded sedimentary/volcanic units (He et al., 1990; Windley et al., 2002) (Fig. 1b). In the northern Chinese Altai, Devonian to Carboniferous meta-sedimentary/volcanic rocks are separated by a normal fault from the rest of the Chinese Altai. The central Chinese Altai is occupied by Cambrian to Silurian marine-facies turbiditic and pyroclastic rocks of the Habahe Group and the Kulumuti Group (Windley et al., 2002), which were interpreted to be an early Paleozoic accretionary complex (Long et al., 2012). Rocks in the central Chinese Altai were metamorphosed up to amphibolite facies, giving rise to dome-shaped metamorphic zonal sequences centered by granitic intrusions (Zhuang, 1994). Late Ordovician to Devonian felsic volcanic rocks of the Dongxileke Formation and marine-facies clastic rocks of the Baihaba Formation unconformably overlie the Habahe Group in the northwestern corner of the Chinese Altai (Fig. 1b) (Long et al., 2010). In the southern Chinese Altai, Devonian volcanic rocks of the Kangbutiebao Formation and the volcanic and sedimentary sequence of the Altai Formation were subjected to high temperature metamorphism, locally up to granulite facies (Wang et al., 2009; Li et al., 2014b). Metamorphic zircons in these rocks yielded both middle Devonian and Permian ages (Long et al., 2007; Jiang et al., 2010; Li et al., 2014b; Wang et al., 2014c; Yang et al., 2015), indicating two episodes of metamorphism. The Irtysh Complex is the southernmost unit of the Chinese Altai. This unit, which mainly contains schist, para- and ortho-gneiss, amphibolite, migmatite, quartzite and chert (Qu and Zhang, 1991; Briggs et al., 2007), was interpreted to represent a Paleozoic accretionary complex (O'Hara et al., 1997; Xiao et al., 2009b). The Irtysh Complex is locally overlain by Permian non-foliated sedimentary and volcanic rocks with an unconformable contact (Fig. 2) (BGMRX, 1978).

The Irtysh Complex in the southern Chinese Altai was strongly deformed by the sinistral Irtysh Shear Zone (Fig. 1b). A mylonitic zone (the Irtysh Fault) in the southern Irtysh Shear Zone (Fig. 1b) was interpreted to be the boundary between the Chinese Altai and the intraoceanic arc system of East/West Junggar in China (Ren et al., 1980). Farther west in Kazakhstan, two sinistral faults, the Chara Shear Zone (also termed the Gornostaev shear zone, Şengör et al., 1993) and North-East Fault (Fig. 1a), splay from the Irtysh Shear Zone (Buslov et al., 2001) (Fig. 1a).

The majority of granitic intrusions in the Chinese Altai (Fig. 1b) are Devonian and Permian in age (Wang et al., 2006; Yuan et al., 2007; Sun et al., 2008; Cai et al., 2011a; Tong et al., 2014). The Devonian granitoids are widely distributed throughout the Chinese Altai and are normally represented by orthogneiss or granitic gneiss, possibly in response to an episode of ridge subduction along an active continental margin (Sun et al., 2009; Cai et al., 2011b). In contrast, the Permian granitoids generally occur in the southern Chinese Altai and are predominantly undeformed (Fig. 1b). These granitoids have been linked to the collision of the Chinese Altai with the arc system of East/West Junggar (e.g. Tong et al., 2014). In addition, the Chinese Altai was intruded by Mesozoic anorogenic granitoids (Li et al., 2013; Wang et al., 2014b).

3. Deformation along the Irtysh Shear Zone

We have mapped a series of ~NW-SE mylonitic zones (Mylonite Zones 1-4) within the Irtysh Shear Zone (Figs. 3-5). Mylonite Zone 1 is normally referred to as the Fuyun-Xibodu Fault that separates the Irtysh Complex from the Altai Formation to the north in the area of Fig. 5, whereas Mylonite Zone 4 is commonly referred to as the Irtysh Fault separating the Irtysh Complex from the Devonian to Carboniferous meta-volcanic/sedimentary rocks of the East Junggar arc system (Figs. 3 and 4). Two additional mylonite zones (Zones 2 and 3) occur between Mylonite Zones 1 and 4 (Figs. 3-5).

The map area was divided into two structural domains with Mylonite Zone 3 as the domain boundary that is roughly close to the Irtysh River. The northern domain is characterized by two folded zones bounded by Mylonite Zones 1-3 (Fig. 5). Rocks in this domain have penetrative axial planar fabric and are dominantly represented by quartzofeldspathic gneiss, which is interlayered with pelitic gneiss/schist, migmatite and amphibolite (Fig. 5). In contrast, the southern domain is bounded by Mylonite Zones 3 and 4, and is characterized by the occurrence of macroscopic fold structures. Lithologically, rocks in the southern domain are represented by interlayered mica schist, banded gneiss, amphibolite, gneissic granitoids and migmatite (Figs. 3 and 4). Dark narrow amphibolite layers can be recognized in a satellite image (Appendix A) and in the field (Figs. 3 and 4), and were used for the structural synthesis.

3.1. Pre-shearing deformation (D_1 and D_2)

3.1.1. D_1

D_1 fabric is locally recognized in the southern domain, where rootless F_2 folds show evidence of folded S_1 (Fig. 6a). The S_1 foliation is illustrated by interlayered dark cleavage domains and microlithons of composite quartz bands. The cleavage domains are occupied by micas that are normally transposed to be sub-parallel with S_2. Garnet porphyroblasts with an internal fabric defined by the alignment of quartz inclusion trails were also recognized. The internal fabric, interpreted as S_1, is oriented at high angle relative to the external S_2 fabric (Fig. 6b).

3.1.2. D_2

S_2 is the dominant foliation in the southern domain of the Irtysh Shear Zone (between Mylonite Zone 3 and Mylonite Zone 4, Figs. 3 and 4). It is parallel to the axial plane of F_2 isoclinal folds (Fig. 6a), and is associated with a stretching lineation that shallowly plunges to ESE (L_2, Figs. 3f and 4f) and is parallel to the strike of the orogenic belt. L_2 is commonly defined by preferred alignment of amphiboles and quartz aggregates (Fig. 6c, d). On a larger scale, S_2 shows variable orientations and defines a series of macroscopic antiforms and synforms (F_3, Section 3.2). Metamorphism associated with D_2 in the southern domain generally exhibits an increasing grade toward the core of the antiforms, where S_2 is commonly associated with migmatization or the growth of high temperature metamorphic minerals (e.g., sillimanite, Fig. 6e).

3.2. Shearing deformation and folding (D_3)

3.2.1. Shearing deformation

Shearing deformation is most evident in the four mylonite zones (Mylonite Zones 1-4). Mylonitic fabric (S_3) within Mylonite Zones 1-3 is steeply dipping to the north (Fig. 5c, e), whereas the mylonitic fabric in Mylonite Zone 4 is sub-vertical, and dips to north or south (Figs. 3c, 4c). Stretching lineation (L_3, Fig. 6f) within each mylonite zone is shallowly plunging to ESE (Figs. 3d, 4d, 5d, f), which together with asymmetric folds, σ-type porphyroblasts, and S-C fabric (Figs. 6g-h and 7a-c), indicates a sinistral-dominant deformation with a reverse component (particularly for Mylonite Zones 1-3). Outcrop-scale folds with hinges subparallel to the stretching lineation (L_3) were also recognized within the mylonite zones, and these folds were interpreted to be A-type folds. Permian granitic dykes (e.g. Zhang et al., 2012) cut Mylonite Zones 2 and 3 (Figs. 3-5), but are displaced by Mylonite Zone 4 in a map view (Fig. 3), indicating multiple stages of sinistral shearing along the Irtysh Shear Zone.

3.2.2. Folding

In the southern domain of the Irtysh Shear Zone, the dominant fabric (S_2) is folded by both outcrop-scale and macroscopic F_3 folds (Figs. 3, 4 and 7d, e). In the hinge zone of macroscopic F_3 folds, S_2 curves progressively without involving intense secondary folds and axial planar fabrics (Figs. 3 and 4), indicating moderate shortening strain during F_3 folding. The hinges of F_3 folds (Figs. 3g and 4g) are sub-parallel to the L_2 stretching lineation (Section 3.1.2). A deflection of L_2 by F_3 folds is locally observed in outcrops (Fig. 7f). On a larger scale, F_3 macroscopic folds were defined by variations in the orientation of S_2, which correspond to a β axis of 11-101 (Fig. 3e) or 33-114 (Fig. 4e). These orientations roughly match the mean orientation of outcrop-scale F_3 fold hinges (B_{32}) in two areas of the southern domain (Figs. 3 and 4), which are 12-102 (Fig. 3g) and 27-120 (Fig. 4g), respectively. We use the β axis of F_3 together with the map-view trace of F_3 to calculate the axial plane (dip angle and dip azimuth) of macroscopic F_3 folds in the southern domain (70-015, Fig. 3h; and 69-037, Fig. 4h).

In the northern domain of the Irtysh Shear Zone, the dominant fabric in two folded zones (Fig. 5a) commonly involves migmatization, and is steeply dipping to NNE with a mean orientation of 77-022 (Fig. 5g). Outcrop-scale folds are predominantly isoclinal (Fig. 7g) with axial planes parallel to the dominant fabric. Stretching lineation associated with the dominant fabric is rarely recognized, unlike the S_2 fabric in the southern domain, which is associated with a well-developed stretching lineation (L_2). In addition, we observed a well-developed shallowly plunging stretching lineation within folded earlier fabrics in the northern domain (Fig. 7h), which is consistent with the characteristics of D_2 structures in the southern domain. Based on these observations, we interpret the dominant fabric in the northern domain to be an axial plane cleavage (S_3) associated with F_3 folding. The ~NNE dipping S_3 fabric in the northern domain is roughly compatible with the axial plane of F_3 (70-015 or 69-037) in the southern domain, thus indicating that F_3 folds in both the northern and southern domains result from the same deformation event. The hinge of outcrop-scale F_3 in the northern domain is shallowly plunging to west (Fig. 5h), which is different from the consistently ESE plunging F_3 in the southern domain.

F_3 structures are cut by Permian ~NE-SE granitic dykes (Figs. 3-5). In the southern domain, granitic dykes show relatively linear features truncating F_3 macroscopic folds (Figs. 3 and 4). Granitic dykes in the northern domain cut the axial plane fabric of F_3 folds, but their orientations show a slight variation from ~NE to ~N-S (Fig. 5).

3.2.3. Relationship between shearing and folding

Our results show that the axial plane of macroscopic F_3 folds in the southern domain and axial planar S_3 fabric in the northern domain are roughly parallel to the mylonitic fabric (S_3). Given the kinematic compatibility, we suggest that F_3 folds developed in association with sinistral-reverse shearing deformation (D_3). This is further supported by constraints on the timing of deformation of the major phase of F_3 folding and D_3 shearing in the late Paleozoic (see Section 5.1). The stretching lineation (L_3) is well developed within the mylonite zones (Mylonite Zones 1-4), but it is weakly developed within the S_3 axial planar fabric in the northern domain. This may suggest that D_3 transpressional deformation was partitioned across the shear zone, with a dominant simple shear component in the mylonite zones and a dominant pure shear component in the fold zones.

4. Geochronology

4.1. Sample description

Two mica schist samples were analyzed by U-Pb zircon geochronology in order to constrain the ages of protoliths within the Irtysh Complex and to provide a maximum time constraint for deformation. A mica schist sample (L14FY04; GPS: 46°58'1.22"N /89°19'21.59"E) was collected from the southern domain of the Irtysh Shear Zone (Fig. 3). The rock has a mineral assemblage of quartz, feldspar and biotite, and shows penetrative S_2 and L_2 fabrics. Sample L14FY137 (GPS: 47°0'26.42"N/89°24'38.02"E) is a garnet mica schist from Mylonite Zone 2 in the northern domain (Fig. 5). This sample mainly comprises quartz, feldspar, garnet and minor oxide, and is characterized by a sinistral mylonitic fabric (S_3).

4.2. Methods

Zircon grains were separated with conventional crushing, heavy liquid and magnetic techniques. The grains were mounted in epoxy resin and polished to expose equatorial section. Cathodoluminescence (CL) images were taken at the Department of Earth Sciences, the University of Hong Kong. Zircon U-Pb geochronology was conducted by employing a Nu Instruments MC-ICP-MS attached to a Resonetics Resolution M-50-HR Excimer Laser

Ablation System at the Department of Earth Sciences, the University of Hong Kong. The analytical procedure and instrument parameters are described in Xia et al. (2011) and Geng et al. (2014). Data processing was done using the ICPMSDataCal software (Liu et al., 2010) and the weighted mean age calculation and concordia plots were done using the ISOPLOT program (Ludwig, 2003).

4.3. Results

Representative CL images of analyzed zircons are shown in Appendix B, and U-Pb analytical results are presented in Appendixes C and D. Concordant ages (<10% discordance) are presented in histogram/probability density plots (Fig. 8). The reported weighted mean $^{206}Pb/^{238}U$ ages of metamorphic zircons from sample L14FY137, which typically have a 0.6% error (95% c.l.), are forced to 1% to account for external errors

Zircons from mica schist (L14FY04) from the southern domain of the Irtysh Shear Zone are characterized by euhedral to subeuhedral shape and oscillatory zoning (Appendix B), indicating a predominant igneous origin. The analyses for this sample yielded two major age peaks of 322 Ma and 342 Ma, and two minor age peaks of 357 Ma and 390 Ma (Fig. 8a), which represent the major populations of detrital zircons in this sample.

Most zircons from the garnet mica schist (L14FY137) show a core-rim structure (Appendix B). The zircon rim shows a dark luminescence without zoning, which together with low Th/U ratios (0.003-0.024), indicates a metamorphic origin. 11 analyses of zircon rims gave a weighted mean age of 295.7±3.0 Ma (MSWD=0.56; Figs. 8b). In contrast, most zircon cores show regular zoning, and a few cores are characterized by dark luminescence with a weak zoning, which together with variable ages, are interpreted to represent a detrital zircon population. The analyses of zircon cores clustered at 326, 341, 358, 392, 406, 444, 472 and 506 Ma (Fig. 8b). Eight additional core analyses yielded Precambrian ages.

5. Discussion

5.1. Protolith ages and timing of deformation

The youngest age obtained from detrital zircons of the two mica schist samples is ~322 Ma. This indicates that the protolith age is younger than ~322 Ma, consistently with the occurrence of a Pennsylvanian fossil assemblage (*Punctatisporites sp., Granulatisporites sp., Calamospora sp., Retusotriletes sp., Lueckisporites sp*) *(BGMRX, 1978)*. Older gneissic granitoids (~450 Ma) have also been reported from the Irtysh Complex (Briggs et al., 2007). This indicates that the Irtysh Complex, which was interpreted to be an accretionary complex (O'Hara et al., 1997; Briggs et al., 2007; Xiao et al., 2009b), incorporated pre-Carboniferous lithostratigraphic associations. Late Carboniferous rocks of the Irtysh Complex contain detrital zircons with similar age peaks (e.g. 444, 472 and 506 Ma) as rocks in the central Chinese Altai (Long et al., 2007), indicating a genetic link of the Irtysh Complex with the rest of the Chinese Altai.

The timing of D_1 and D_2 remains poorly constrained, but must be younger than the ~322 Ma detrital zircon age. A large number of geochronological data have been reported along the Irtysh Shear Zone to constrain the timing of sinistral shearing (D_3). In Kazakhstan, the sinistral deformation was constrained to ~290-265 Ma based on $^{40}Ar/^{39}Ar$ cooling ages of hornblende, muscovite and biotite from the shear zone (Buslov et al., 2004b, and references therein). An undeformed granodiorite intruded into the Kazakhstan segment of the Irtysh Shear Zone, yielded a zircon U-Pb age of ~252 Ma (Zhang et al., 2012), thus providing a minimum age constraint on the timing of shearing. The D_3 shearing in the Chinese segment of the Irtysh Shear Zone was constrained at an age range of ~290-244 Ma, which was mainly based on $^{40}Ar/^{39}Ar$ cooling ages of rocks along the shear zone (Fig. 2) (Laurent-Charvet et al., 2003; Yan et al., 2004; Briggs et al., 2007; Briggs et al., 2009; Zhang et al., 2012; Li et al., 2015b). These ages roughly overlap with chronological constraints from the Kazakhstan segment of the Irtysh Shear Zone. Our structural observations are indicative of two stages of sinistral shearing (D_3). The early phase of shearing occurred prior to the occurrence of ~NE-SW granitic dykes that cut Mylonite Zones 2 and 3 (Figs. 3 and 4). A later phase of shearing is recorded by Mylonite Zone 4, which cut the granitic dykes (Fig. 3). The published ages of these granitic dykes have a large range, but variably clustered at ~252 Ma (Zhang et al., 2012) and 298-274 Ma (Briggs et al., 2007). We suggest that these ages constrain the early phase of D_3 shearing, which terminated prior to ~252 Ma. New metamorphic zircons from Mylonite Zone 2 yielded an age of ~295 Ma, which given the poor constraint on the growth of metamorphic zircons with respect to the deformation fabrics, is interpreted to represent the timing of either D_2 or D_3.

Overall, available geochronological data suggest that D_1-D_2 of the Irtysh Shear Zone occurred after ~322 Ma but before ~290 Ma, and the major phase of D_3 sinistral shearing may have occurred in the Permian (~290-252 Ma). Both F_3 macroscopic folds in the southern domain of the Irtysh Shear Zone and F_3 axial plane fabric in the northern domain are cut by the relatively linear granitic dykes (Figs. 3-5; Section 3.2.2) that constrain the major phase of F_3 folding to pre- ~252 Ma. This time constraint is consistent with the observation that F_3 folding involves an axial plane fabric associated with migmatization, which indicates high temperature conditions during F_3 that evolved into a more brittle setting prior to the intrusion of granitic dykes in ~252 Ma. Pre-Mesozoic F_3 folding are overlapped in time with the major phase of sinistral shearing in the Permian, further supporting the interpretation that D_3 transpressional deformation occurred in the late Paleozoic.

Based on our data, the role of Mesozoic to Cenozoic reactivation of D_3 structures is poorly constrained. Apatite fission track data record fast cooling of basement rocks within the Kazakhstan segment of the Irtysh Shear Zone in the Late Cretaceous (~100-70) and Late Oligocene (~25 Ma), which were interpreted to reflect the reactivation of the Irtysh Shear Zone (Glorie et al., 2012b). In the Chinese Altai, apatite fission track data from Paleozoic basement rocks to the north of the Irtysh Shear Zone also show fast cooling during the Cretaceous and Cenozoic (~Miocene), possibly as a result of increased uplift and erosion of the Altai Mountains (Yuan et al., 2006). The role of the Chinese segment of the Irtysh Shear Zone in response to these uplift events remains enigmatic. Our structural observations show sinistral shearing of Mylonite Zone 4 after the Permian, which was possibly associated with the Cretaceous and Cenozoic uplift events. Permian granitic dykes show slight strike variations (Fig. 5; Section 3.2.2), which either represent a primary structure or a later folding event.

5.2. Structural evolution of the Irtysh Shear Zone

Three episodes of deformation (D_1 - D_3) were recognized within the Irtysh Shear Zone. The earliest deformation (D_1) is strongly overprinted by D_2, so the geometry of its associated structures (e.g., F_1 folds) remains unknown. The orientation of S_2 prior to D_3 was likely shallowly dipping based on the observations of shallowly plunging F_3 fold hinges (B_{32}) (Figs. 3e, g and 4e, g), steeply dipping F_3 axial planes (Figs. 3h and 4h), and nearly-symmetric F_3 macroscopic folds (Figs. 3 and 4). The original shallowly dipping S_2, together with the evidence for shallowly plunging L_2, which is oriented ~NW-SE subparallel to the orogenic strike, suggest that this fabric formed by sub-vertical flattening and orogen-parallel stretching during D_2. Similar observations of flat-lying foliations and orogen-parallel stretching lineations were recognized in other orogens (such as the Himalayan Orogen and the Eastern Alps; Brun et al., 1985; Frisch et al., 2000; Scharf et al., 2013; Xu et al., 2013), and were attributed to orogen-parallel extension possibly driven by gravitational potential energy (e.g. Dewey, 1988; Selverstone, 2004). Accordingly, we interpret D_2 structures to represent a phase of orogen-parallel extension associated with the collapse of an over-thickened orogen. In the context of this explanation, D_1 can be interpreted as a contractional phase of deformation that led to crustal-thickening prior to D_2 extension.

D_3 in the Irtysh Shear Zone was characterized by transpressional deformation, which was partitioned into orogen-parallel shearing and orogen-perpendicular folding. The overall geometry of the Irtysh Shear Zone in the Fuyun area (i.e., D_3 structures, Fig. 9a) is consistent with the observations by Qu and Zhang (1991; 1994), who described a series of NW-SE folded zones bounded by mylonite zones. Briggs et al. (2007) measured a striation at 65-340 on a local oblique fault of 72-055 (pitching 65° to north; based on one measurement) within the Irtysh Shear Zone (Fig. 2), and thus these authors interpreted the Irtysh Shear Zone to be a SW-directed thrust belt. We note, however, that the oblique reverse fault observed by Briggs et al. (2007) is located in a restraining bend zone of Mylonite Zone 4 (Figs. 2, 3 and 4), where one structural measurement may not be representative for the kinematics of the shear zone. Furthermore, sinistral shearing fabrics with sub-horizontal stretching lineations were observed along the whole southern Chinese Altai from the Qinhe area, through the Fuyun area (this study), to the Chonghuer area (Fig. 1b) (Laurent-Charvet et al., 2002; Laurent-Charvet et al., 2003; Jiang et al., 2015; Zhang et al., 2015), consistently showing sinistral kinematics of the shear zone.

The timing of major phase of deformation of the Irtysh Shear Zone (~322-252 Ma) roughly overlaps with the convergence between the Chinese Altai and the intra-oceanic arc system of the East/West Junggar (Cai et al., 2012; Li et al., 2014a; Li et al., 2015a). The youngest subduction-related igneous rocks in the Chinese Altai yielded an age of ~313±13 Ma (Cai et al., 2012), which is roughly consistent with the youngest age peak of the accretionary complex (i.e. Irtysh Complex) at ~322 Ma, suggesting that closure of the Ob-Zaisan Ocean between the Chinese Altai and the East/West Junggar took place in the late Carboniferous. Therefore, we interpret that D_1-D_3 of the Irtysh Shear Zone in the Fuyun area represents three stages of convergence of the Chinese Altai with the East Junggar, which is characterized by a cycle of crustal thickening (D_1), extensional collapse (D_2) and transpressional thickening (D_3) (Fig. 9b). Alternatively, the whole convergence process was possibly oblique, involving oblique convergence during D_1 and D_3, between which D_2 represents an intermittent episode of orogen-parallel extension.

On a larger scale, the Irtysh Shear Zone activated during the convergence of the peri-Siberian orogenic system (the Chinese Altai) and the Kazakhstan orogenic system (Fig. 1a). Sinistral deformation of the Irtysh Shear Zone (D_3), together with the other shear zones (i.e. Chara Shear Zone and North-East Shear Zone, Fig. 1a), accommodates the left-lateral displacement of the peri-Siberian orogenic system with respect to the Kazakhstan orogenic system. In contrast, a large number of shear zones developed to the south of the Irtysh Shear Zone with right-lateral displacement (Shu et al., 1999; Laurent-Charvet et al., 2003; Wang et al., 2008; Lin et al., 2009; Wang et al., 2010; Wang et al., 2014a). Available chronological data constrain the dextral shearing in an age range of ~290-240 Ma (Shu et al., 1999; Laurent-Charvet et al., 2003; Wang et al., 2014a), which overlaps with sinistral deformation of the Irtysh Shear Zone. Coeval dextral and sinistral shearing accommodates the eastward migration of the internal orogenic segments within the Kazakhstan orogenic system in the late Paleozoic (e.g., the West Junggar-North Tianshan segment, Figs. 1a and 10).

The geodynamic driving mechanism that led to lateral migration of internal segments of the Kazakhstan orogenic system in the late Paleozoic remains enigmatic. Previous studies have proposed that the late Paleozoic wretch tectonics was possibly genetically linked with the late Paleozoic convergence of Baltica, Tarim and Siberian cratons (e.g., Choulet et al., 2011). Indeed, the closure of the paleo-Asian Ocean and the following continental convergence occurred simultaneously with the late Paleozoic wretch tectonics. The Ob-Zaisan Ocean, between the peri-Siberian and the Kazakhstan orogenic systems, may have been closed since the late Carboniferous as discussed above. In the southwestern CAOB, the closure of the South Tianshan Ocean, between the Kazakhstan orogenic system and the Tarim Craton, is possibly dischronous, initiating in the late Carboniferous and lasting until Early Triassic (Han et al., 2011; Xiao et al., 2013; Alexeiev et al., 2015). To the west, the collision between the Kazakhstan orogenic system and the Baltica Craton initiated in the middle to late Carboniferous (Filippova et al., 2001; Windley et al., 2007). Given the time overlap between strike-slip faulting and the continental assembly, we consider that the lateral migration of the West Junggar-North Tianshan segment and the Yili Block (Fig. 1a), assisted by strike-slip shearing, occurred during the assembly/collision of the Siberian, Baltica and Tarim cratons, to adjust relative movements of these cratons. A lateral extrusion model has been proposed to explain the coeval dextral and sinistral shearing in the western CAOB in the late Paleozoic

(Wang et al., 2008), similarly as the lateral escape of SE Asia in response to the India-Asian collision (Tapponnier and Molnar, 1976; Tapponnier et al., 1982). However, we consider that the late Paleozoic amalgamation of the western CAOB involves the assembly of three continental cratons of Siberia, Tarim and Baltica at a similar time, which is not comparable to the escape tectonics associated with the indentation of the Indian plate into the Asia (e.g. Tapponnier et al., 1982). Alternatively, the eastward migration of orogenic segments of the western CAOB was possibly associated with the coeval convergence of Siberian, Tarim and Baltica cratons in the late Paleozoic, during which the ongoing subduction in the eastern CAOB could provide spatial freedom for the material migration towards east (Fig. 10). However, this model is based only on limited chronological and structural data, and further work, particularly on the kinematics and timing of major faults in Kazakhstan, is required.

In the Mesozoic to Cenozoic, the Irtysh Shear Zone and other Paleozoic structures in the western CAOB were reactivated, possibly as a result of the far-field response to collision of the Cimmerian terrane and India with the southern margin of Eurasia (Dumitru et al., 2001; De Grave et al., 2007; Glorie and De Grave, 2015). Under this tectonic interpretation, the Chinese Altai was subject to ~NE-SW shortening in the Mesozoic to Cenozoic. The ~NW-SE F_3 folds of the Irtysh Shear Zone are compatible with ~NE-SW shortening, but it is unclear whether F_3 macroscopic folds were amplified in the Mesozoic to Cenozoic to accommodate this shortening. Given the evidence that the major phase of F_3 folding occurred prior to Mesozoic (Section 5.1), it is concluded that such fold amplification must have been limited. Alternatively, ~NE-SW shortening in the Mesozoic to Cenozoic may have been accommodated by a series of ~NW-SE reverse faults in the southern Chinese Altai (Fig. 2).

6. Conclusions

Three episodes of late Paleozoic deformation were recognized for the Chinese segment of the Irtysh Shear Zone in Central Asia. S_1 is locally recognized and transposed to be parallel to S_2. S_2 was shallowly dipping prior to D_3 and associated with ~NW-SE shallowly plunging stretching lineation that is subparallel to the orogenic strike, and thus was interpreted to represent an orogen-parallel extensional event. D_3 is characterized by transpressional deformation, which is represented by a series of sinistral mylonitic zones and bounded F_3 fold zones. Chronological data constrain D_1-D_2 and major phase of D_3 within a time range of ~322-252 Ma, and a later phase of reactivation of D_3 structures may have occurred in the Mesozoic to Cenozoic. Late Paleozoic activity of D_1-D_3 is overlapped in time with the convergence between the Chinese Altai and the East Junggar. Therefore, we interpret that late Paleozoic deformation of the Irtysh Shear Zone represents three stages of convergence of the Chinese Altai with the East Junggar, which was characterized by a cycle of crustal thickening (D_1), extensional collapse (D_2), and transpressional thickening (D_3). On a larger scale, sinistral shearing (D_3) in the late Paleozoic, together with dextral shearing farther south, accommodated the eastward migration of internal orogenic segments of the western CAOB, possibly associated with the amalgamation of multiple arc systems and continental blocks during the late Paleozoic.

Acknowledgements: This study was financially supported by the Major Basic Research Project of the Ministry of Science and Technology of China (Grant: 2014CB448000 and 2014CB440801), Hong Kong Research Grant Council (HKU705311P and HKU704712P), National Science Foundation of China (41273048), HKU CRCG grants and a HKU small grant (201309176226). We thank Rod Holcombe for the discussion with the structural interpretation, and Jianhua Li and Arnaud Broussolle for the helpful comments. Jean Wong and Hongyan Geng are acknowledged for their help during the geochronological analysis. This work is a contribution of the Joint Laboratory of Chemical Geodynamics between HKU and CAS (Guangzhou Institute of Geochemistry), IGCP 592 and PROCORE France/Hong Kong Joint Research Scheme.

References

Alexeiev, D.V., Cook, H.E., Buvtyshkin, V.M., Golub, L.Y., 2009. Structural evolution of the Ural–Tian Shan junction: A view from Karatau ridge, South Kazakhstan. Comptes Rendus Geoscience 341, 287-297.

Alexeiev, D.V., Biske, Y.S., Wang, B., Djenchuraeva, A.V., Getman, O.F., Aristov, V.A., Kröner, A., Liu, H., Zhong, L., 2015. Tectono-Stratigraphic framework and Palaeozoic evolution of the Chinese South Tianshan. Geotectonics 49, 93-122.

Allen, M.B., Şengör, A.M.C., Natal'in, B.A., 1995. Junggar, Turfan and Alakol basins as Late Permian to ?Early Triassic extensional structures in a sinistral shear zone in the Altaid orogenic collage, Central Asia. Journal of the Geological Society 152, 327-338.

Allen, M.B., Alsop, G.I., Zhemchuzhnikov, V.G., 2001. Dome and basin refolding and transpressive inversion along the Karatau Fault System, southern Kazakstan. Journal of the Geological Society 158, 83-95.

Amante, C., Eakins, B.W., 2009. ETOPO1 1 arc-minute global relief model: procedures, data sources and analysis. NOAA Technical Memorandum NESDIS NGDC-24. 19 pp

Bazhenov, M.L., Levashova, N.M., Degtyarev, K.E., Van der Voo, R., Abrajevitch, A.V., McCausland, P.J.A., 2012. Unraveling the early–middle Paleozoic paleogeography of Kazakhstan on the basis of Ordovician and Devonian paleomagnetic results. Gondwana Research 22, 974-991.

BGMRX, 1978. Geological Map of the Fuyun Sheet: scale 1:200,000. Unpublished.

Briggs, S.M., Yin, A., Manning, C.E., Chen, Z.-L., Wang, X.-F., Grove, M., 2007. Late Paleozoic tectonic history of the Ertix Fault in the Chinese Altai and its implications for the development of the Central Asian Orogenic System. Geological Society of America Bulletin 119, 944-960.

Briggs, S.M., Yin, A., Manning, C.E., Chen, Z.-L., Wang, X.-F., 2009. Tectonic development of the southern Chinese Altai Range as determined by structural geology, thermobarometry, 40Ar/39Ar thermochronology, and Th/Pb ion-microprobe monazite geochronology. Geological Society of America Bulletin 121, 1381-1393.

Brun, J.-P., Burg, J.-P., Ming, C.G., 1985. Strain trajectories above the Main Central Thrust (Himalaya) in southern Tibet. Nature 313, 388-390.

Buslov, M.M., Saphonova, I.Y., Watanabe, T., Obut, O., Fujiwara, Y., Iwata, K., Semakov, N., Sugai, Y., Smirnova, L., Kazansky, A.Y., 2001. Evolution of the Paleo-Asian Ocean (Altai-Sayan Region, Central Asia) and collision of possible Gondwana-derived terranes with the southern marginal part of the Siberian continent. Geosciences Journal 5, 203-224.

Buslov, M.M., Fujiwara, Y., Iwata, K., Semakov, N.N., 2004a. Late Paleozoic-Early Mesozoic Geodynamics of Central Asia. Gondwana Research 7, 791-808.

Buslov, M.M., Watanabe, T., Fujiwara, Y., Iwata, K., Smirnova, L.V., Safonova, I.Y., Semakov, N.N., Kiryanova, A.P., 2004b. Late Paleozoic faults of the Altai region, Central Asia: tectonic pattern and model of formation. Journal of Asian Earth Sciences 23, 655-671.

Cai, K., Sun, M., Yuan, C., Zhao, G., Xiao, W., Long, X., Wu, F., 2011a. Prolonged magmatism, juvenile nature and tectonic evolution of the Chinese Altai, NW China: Evidence from zircon U–Pb and Hf isotopic study of Paleozoic granitoids. Journal of Asian Earth Sciences 42, 949-968.

Cai, K., Sun, M., Yuan, C., Zhao, G., Xiao, W., Long, X., Wu, F., 2011b. Geochronology, petrogenesis and tectonic significance of peraluminous granites from the Chinese Altai, NW China. LITHOS 127, 261-281.

Cai, K., Sun, M., Yuan, C., Xiao, W., Zhao, G., Long, X., Wu, F., 2012. Carboniferous mantle-derived felsic intrusion in the Chinese Altai, NW China: Implications for geodynamic change of the accretionary orogenic belt. Gondwana Research 22, 681-698.

Chen, J.-F., Han, B.-F., Ji, J.-Q., Zhang, L., Xu, Z., He, G.-Q., Wang, T., 2010. Zircon U–Pb ages and tectonic implications of Paleozoic plutons in northern West Junggar, North Xinjiang, China. LITHOS 115, 137-152.

Chen, S., Pe-Piper, G., Piper, D.J.W., Guo, Z., 2014. Ophiolitic mélanges in crustal-scale fault zones: Implications for the Late Palaeozoic tectonic evolution in West Junggar, China.

Tectonics, 2013TC003488.

Choulet, F., Chen, Y., Wang, B., Faure, M., Cluzel, D., Charvet, J., Lin, W., Xu, B., 2011. Late Paleozoic paleogeographic reconstruction of Western Central Asia based upon paleomagnetic data and its geodynamic implications. Journal of Asian Earth Sciences 42, 867-884.

Choulet, F., Cluzel, D., Faure, M., Lin, W., Wang, B., Chen, Y., Wu, F.Y., Ji, W., 2012. New constraints on the pre-Permian continental crust growth of Central Asia (West Junggar, China) by U–Pb and Hf isotopic data from detrital zircon. Terra Nova 24, 189-198.

De Grave, J., Buslov, M.M., Van den haute, P., 2007. Distant effects of India–Eurasia convergence and Mesozoic intracontinental deformation in Central Asia: Constraints from apatite fission-track thermochronology. Journal of Asian Earth Sciences 29, 188-204.

Dewey, J.F., 1988. Extensional collapse of orogens. Tectonics 7, 1123-1139.

Dumitru, T.A., Zhou, D., Chang, E.Z., Graham, S.A., Hendrix, M.S., Sobel, E.R., Carroll, A.R., 2001. Uplift, exhumation, and deformation in the Chinese Tian Shan, in: Hendrix, M.S., Davis, G.A. (Eds.), Paleozoic and Mesozoic tectonic evolution of central and eastern Asia - from continental assembly to intracontinental deformation. Geological Society of America Memoir 194, pp. 71-100.

Eizenhöfer, P.R., Zhao, G., Zhang, J., Sun, M., 2014. Final closure of the Paleo-Asian Ocean along the Solonker Suture Zone: Constraints from geochronological and geochemical data of Permian volcanic and sedimentary rocks. Tectonics 33, 441-463.

Filippova, I., Bush, V., Didenko, A., 2001. Middle Paleozoic subduction belts: the leading factor in the formation of the Central Asian fold-and-thrust belt. Russian Journal of Earth Sciences 3, 405-426.

Frisch, W., Dunkl, I., Kuhlemann, J., 2000. Post-collisional orogen-parallel large-scale extension in the Eastern Alps. Tectonophysics 327, 239-265.

Geng, H., Brandl, G., Sun, M., Wong, J., Kröner, A., 2014. Zircon ages defining deposition of the Palaeoproterozoic Soutpansberg Group and further evidence for Eoarchaean crust in South Africa. Precambrian Research 249, 247-262.

Glorie, S., De Grave, J., Buslov, M., Zhimulev, F., Stockli, D., Batalev, V., Izmer, A., Vanhaecke, F., Elburg, M., 2011a. Tectonic history of the Kyrgyz South Tien Shan (Atbashi-Inylchek) suture zone: The role of inherited structures during deformation-propagation. Tectonics 30, TC6016, doi:6010.1029/2011TC002949.

Glorie, S., De Grave, J., Buslov, M.M., Zhimulev, F.I., Izmer, A., Vandoorne, W., Ryabinin, A., Van den haute, P., Vanhaecke, F., Elburg, M.A., 2011b. Formation and Palaeozoic evolution of the Gorny-Altai–Altai-Mongolia suture zone (South Siberia): Zircon U/Pb constraints on the igneous record. Gondwana Research 20, 465-484.

Glorie, S., De Grave, J., Buslov, M.M., Zhimulev, F.I., Elburg, M.A., Van den haute, P., 2012a. Structural control on Meso-Cenozoic tectonic reactivation and denudation in the Siberian Altai: Insights from multi-method thermochronometry. Tectonophysics 544–545, 75-92.

Glorie, S., De Grave, J., Delvaux, D., Buslov, M.M., Zhimulev, F.I., Vanhaecke, F., Elburg, M.A., Van den haute, P., 2012b. Tectonic history of the Irtysh shear zone (NE Kazakhstan): New constraints from zircon U/Pb dating, apatite fission track dating and palaeostress analysis. Journal of Asian Earth Sciences 45, 138-149.

Glorie, S., De Grave, J., 2015. Exhuming the Meso–Cenozoic Kyrgyz Tianshan and Siberian Altai-Sayan: A review based on low-temperature thermochronology. Geoscience Frontiers.

Han, B.-F., He, G.-Q., Wang, X.-C., Guo, Z.-J., 2011. Late Carboniferous collision between the Tarim and Kazakhstan–Yili terranes in the western segment of the South Tian Shan Orogen, Central Asia, and implications for the Northern Xinjiang, western China. Earth-Science Reviews 109, 74-93.

Han, Y., Zhao, G., Sun, M., Eizenhöfer, P.R., Hou, W., Zhang, X., Liu, D., Wang, B., Zhang, G., 2015. Paleozoic accretionary orogenesis in the Paleo-Asian Ocean: Insights from detrital zircons from Silurian to Carboniferous strata at the northwestern margin of the Tarim Craton. Tectonics 34, doi:10.1002/2014TC003668.

He, G., Han, B., Yue, Y., Wang, J., 1990. Tectonic division and crustal evolution of Altay orogenic belt in China. Geoscience of Xinjiang 2, 9-20 (In Chinese with the English abstract).

Jahn, B.-M., Wu, F., Chen, B., 2000. Granitoids of the Central Asian Orogenic Belt and continental growth in the Phanerozoic. Transactions of the Royal Society of Edinburgh Earth Sciences 91, 181-193.

Jahn, B.-M., 2004. The Central Asian Orogenic Belt and growth of the continental crust in the Phanerozoic. Geological Society, London, Special Publications 226, 73-100.

Jiang, Y., Sun, M., Zhao, G., Yuan, C., Xiao, W., Xia, X., Long, X., Wu, F., 2010. The ~ 390 Ma high-T metamorphic event in the Chinese Altai: A consequence of ridge-subduction? American Journal of Science 310, 1421-1452.

Jiang, Y., Štípská, P., Sun, M., Schulmann, K., Zhang, J., Wu, Q.H., Long, X., Yuan, C., Racek, M., Zhao, G., Xiao, W., 2015. Juxtaposition of Barrovian and migmatite domains in the Chinese Altai: a result of crustal thickening followed by doming of partially molten lower crust. Journal of Metamorphic Geology 33, 45-70.

Jolivet, M., Ritz, J.-F., Vassallo, R., Larroque, C., Braucher, R., Todbileg, M., Chauvet, A., Sue, C., Arnaud, N., De Vicente, R., Arzhanikova, A., Arzhanikov, S., 2007. Mongolian summits: An uplifted, flat, old but still preserved erosion surface. Geology 35, 871-874.

Jolivet, M., De Boisgrollier, T., Petit, C., Fournier, M., Sankov, V., Ringenbach, J.C., Byzov, L., Miroshnichenko, A., Kovalenko, S.N., Anisimova, S., 2009. How old is the Baikal Rift Zone? Insight from apatite fission track thermochronology. Tectonics 28.

Jolivet, M., Dominguez, S., Charreau, J., Chen, Y., Li, Y., Wang, Q., 2010. Mesozoic and Cenozoic tectonic history of the Central Chinese Tian Shan: Reactivated tectonic structures and active deformation. Tectonics 29.

Khain, E., Bibikova, E., Kröner, A., Zhuravlev, D., Sklyarov, E., Fedotova, A., Kravchenko-Berezhnoy, I., 2002. The most ancient ophiolite of the Central Asian fold belt: U–Pb and Pb–Pb zircon ages for the Dunzhugur Complex, Eastern Sayan, Siberia, and geodynamic implications. Earth and Planetary Science Letters 199, 311-325.

Kröner, A., Lehmann, J., Schulmann, K., Demoux, A., Lexa, O., Tomurhuu, D., Štípská, P., Liu, D., Wingate, M.T., 2010. Lithostratigraphic and geochronological constraints on the evolution of the Central Asian Orogenic Belt in SW Mongolia: Early Paleozoic rifting followed by late Paleozoic accretion. American Journal of Science 310, 523-574.

Kröner, A., Kovach, V., Belousova, E., Hegner, E., Armstrong, R., Dolgopolova, A., Seltmann, R., Alexeiev, D.V., Hoffmann, J.E., Wong, J., Sun, M., Cai, K., Wang, T., Tong, Y., Wilde, S.A., Degtyarev, K.E., Rytsk, E., 2014. Reassessment of continental growth during the accretionary history of the Central Asian Orogenic Belt. Gondwana

Research 25, 103-125.

Laurent-Charvet, S., Charvet, J., Shu, L., Ma, R., Lu, H., 2002. Palaeozoic late collisional strike-slip deformations in Tianshan and Altay, Eastern Xinjiang, NW China. Terra Nova 14, 249-256.

Laurent-Charvet, S., Charvet, J., Monié, P., Shu, L., 2003. Late Paleozoic strike-slip shear zones in eastern Central Asia (NW China): New structural and geochronological data. Tectonics 22.

Lehmann, J., Schulmann, K., Lexa, O., Corsini, M., Kröner, A., Štípská, P., Tomurhuu, D., Otgonbator, D., 2010. Structural constraints on the evolution of the Central Asian Orogenic Belt in SW Mongolia. American Journal of Science 310, 575-628.

Levashova, N.M., Mikolaichuk, A.V., McCausland, P.J.A., Bazhenov, M.L., Van der Voo, R., 2007. Devonian paleomagnetism of the North Tien Shan: Implications for the middle-Late Paleozoic paleogeography of Eurasia. Earth and Planetary Science Letters 257, 104-120.

Li, D., He, D., Santosh, M., Tang, J., 2014a. Petrogenesis of Late Paleozoic volcanics from the Zhaheba depression, East Junggar: Insights into collisional event in an accretionary orogen of Central Asia. LITHOS 184, 167-193.

Li, D., He, D., Ma, D., Tang, Y., Kong, Y., Tang, J., 2015a. Carboniferous–Permian tectonic framework and its later modifications to the area from eastern Kazakhstan to southern

Altai: Insights from the Zaysan–Jimunai Basin evolution. Journal of Asian Earth Sciences, in press.

Li, P., Yuan, C., Sun, M., Long, X., Cai, K., 2015b. Thermochronological constraints on the late Paleozoic tectonic evolution of the southern Chinese Altai. Journal of Asian Earth Sciences, in press.

Li, S., Wang, T., Wilde, S.A., Tong, Y., 2013. Evolution, source and tectonic significance of Early Mesozoic granitoid magmatism in the Central Asian Orogenic Belt (central segment). Earth-Science Reviews 126, 206-234.

Li, Z., Yang, X., Li, Y., Santosh, M., Chen, H., Xiao, W., 2014b. Late Paleozoic tectono–metamorphic evolution of the Altai segment of the Central Asian Orogenic Belt: Constraints from metamorphic P–T pseudosection and zircon U–Pb dating of ultra-high-temperature granulite. LITHOS 204, 83-96.

Lin, W., Faure, M., Shi, Y., Wang, Q., Li, Z., 2009. Palaeozoic tectonics of the south-western Chinese Tianshan: new insights from a structural study of the high-pressure/low-temperature metamorphic belt. International Journal of Earth Sciences 98, 1259-1274.

Liu, Y., Gao, S., Hu, Z., Gao, C., Zong, K., Wang, D., 2010. Continental and Oceanic Crust Recycling-induced Melt–Peridotite Interactions in the Trans-North China Orogen: U–Pb Dating, Hf Isotopes and Trace Elements in Zircons from Mantle Xenoliths. Journal of Petrology 51, 537-571.

Long, X., Sun, M., Yuan, C., Xiao, W., Lin, S., Wu, F., Xia, X., Cai, K., 2007. Detrital zircon age and Hf isotopic studies for metasedimentary rocks from the Chinese Altai: Implications for the Early Paleozoic tectonic evolution of the Central Asian Orogenic Belt. Tectonics 26.

Long, X., Yuan, C., Sun, M., Xiao, W., Zhao, G., Wang, Y., Cai, K., Xia, X., Xie, L., 2010. Detrital zircon ages and Hf isotopes of the early Paleozoic flysch sequence in the Chinese Altai, NW China: new constrains on depositional age, provenance and tectonic evolution. Tectonophysics 480, 213-231.

Long, X., Yuan, C., Sun, M., Xiao, W., Wang, Y., Cai, K., Jiang, Y., 2012. Geochemistry and Nd isotopic composition of the Early Paleozoic flysch sequence in the Chinese Altai, Central Asia: Evidence for a northward-derived mafic source and insight into Nd model ages in accretionary orogen. Gondwana Research 22, 554-566.

Ludwig, K.R., 2003. Isoplot/Ex Version 3.0: A geochronological toolkit for Microsoft Excel. Berkeley. 70 pp

Natal'in, B.A., Şengör, A.C., 2005. Late Palaeozoic to Triassic evolution of the Turan and Scythian platforms: the pre-history of the Palaeo-Tethyan closure. Tectonophysics 404, 175-202.

O'Hara, K.D., Yang, X.-Y., Guoyuan, X., Li, Z., 1997. Regional δ18O gradients and fluid-rock interaction in the Altay accretionary complex, northwest China. Geology 25, 443-446.

Qu, G., 1991. Deformational structure of tectonic division of the Altaides, Xinjiang. Geoscience of Xinjiang 3, 132-144 (in Chinese with the English abstract).

Qu, G., Zhang, J., 1991. Irtys structural zone. Geoscience of Xinjiang 3, 115-131 (in Chinese with the English abstract).

Qu, G., Zhang, J., 1994. Oblique thrust systems in the Altay orogen, China. Journal of Southeast Asian Earth Sciences 9, 277-287.

Ren, J.S., Jiang, C.F., Zhang, Z.K., Qin, D.Y., 1980. Geotectonic Evolution of China. Science Press, Beijing. 124 pp

Rolland, Y., Alexeiev, D.V., Kröner, A., Corsini, M., Loury, C., Monié, P., 2013. Late Palaeozoic to Mesozoic kinematic history of the Talas–Ferghana strike-slip fault (Kyrgyz West Tianshan) as revealed by 40Ar/39Ar dating of syn-kinematic white mica. Journal of Asian Earth Sciences 67–68, 76-92.

Safonova, I., 2013. The Russian-Kazakh Altai orogen: An overview and main debatable issues. Geoscience Frontiers, 537-552.

Scharf, A., Handy, M.R., Favaro, S., Schmid, S.M., Bertrand, A., 2013. Modes of orogen-parallel stretching and extensional exhumation in response to microplate indentation and roll-back subduction (Tauern Window, Eastern Alps). International

Journal of Earth Sciences 102, 1627-1654.

Selverstone, J., 2004. Are the Alps collapsing? Annual Review of Earth and Planetary Sciences 33, 113.

Şengör, A.M.C., Natal'in, B.A., Burtman, V.S., 1993. Evolution of the Altaid tectonic collage and Palaeozoic crustal growth in Eurasia. Nature 364, 299-307.

Şengör, A.M.C., Natal'in, B.A., 1996. Turkic-type orogeny and its role in the making of the continental crust. Annual Review of Earth and Planetary Sciences 24, 263-337.

Shu, L., Charvet, J., Guo, L., Lu, H., Laurent-Charvet, S., 1999. A large-scale Palaeozoic dextral ductile strike-slip zone: the Aqqikkudug-Weiya zone along the northern margin of the central Tianshan Belt, Xinjiang, NW China. Acta Geologica Sinica 73, 148-162.

Sun, M., Yuan, C., Xiao, W., Long, X., Xia, X., Zhao, G., Lin, S., Wu, F., Kröner, A., 2008. Zircon U–Pb and Hf isotopic study of gneissic rocks from the Chinese Altai: progressive accretionary history in the early to middle Palaeozoic. Chemical Geology 247, 352-383.

Sun, M., Long, X., Cai, K., Jiang, Y., Wang, B., Yuan, C., Zhao, G., Xiao, W., Wu, F., 2009. Early Paleozoic ridge subduction in the Chinese Altai: insight from the abrupt change in zircon Hf isotopic compositions. Science in China Series D: Earth Sciences 52, 1345-1358.

Tapponnier, P., Molnar, P., 1976. Slip-line field theory and large-scale continental tectonics. Nature 264, 319-324.

Tapponnier, P., Peltzer, G., Le Dain, A.Y., Armijo, R., Cobbold, P., 1982. Propagating extrusion tectonics in Asia: New insights from simple experiments with plasticine. Geology 10, 611-616.

Tong, Y., Wang, T., Jahn, B.M., Sun, M., Hong, D.W., Gao, J.F., 2014. Post-accretionary permian granitoids in the Chinese Altai orogen: Geochronology, petrogenesis and tectonic implications. American Journal of Science 314, 80-109.

Van der Voo, R., 2004. Paleomagnetism, oroclines, and growth of the continental crust. GSA Today 14, 4–9.

Van der Voo, R., van Hinsbergen, D.J., Domeier, M., Spakman, W., Torsvik, T.H., 2015. Latest Jurassic–earliest Cretaceous closure of the Mongol-Okhotsk Ocean: A paleomagnetic and seismological-tomographic analysis. Geological Society of America Special Papers 513, doi:10.1130/2015.2513(1119).

Vassallo, R., Jolivet, M., Ritz, J.-F., Braucher, R., Larroque, C., Sue, C., Todbileg, M., Javkhlanbold, D., 2007. Uplift age and rates of the Gurvan Bogd system (Gobi-Altay) by apatite fission track analysis. Earth and Planetary Science Letters 259, 333-346.

Vladimirov, A., Kruk, N., Khromykh, S., Polyansky, O., Chervov, V., Vladimirov, V., Travin, A., Babin, G., Kuibida, M., Vladimirov, V., 2008. Permian magmatism and lithospheric deformation in the Altai caused by crustal and mantle thermal processes. Russian Geology and Geophysics 49, 468-479.

Wang, B., Faure, M., Shu, L., de Jong, K., Charvet, J., Cluzel, D., Jahn, B.m., Chen, Y., Ruffet, G., 2010. Structural and geochronological study of high-pressure metamorphic rocks in the Kekesu section (northwestern China): Implications for the late Paleozoic tectonics of the Southern Tianshan. The Journal of Geology 118, 59-77.

Wang, B., Cluzel, D., Jahn, B.-m., Shu, L., Chen, Y., Zhai, Y., Branquet, Y., Barbanson, L., Sizaret, S., 2014a. Late Paleozoic pre-and syn-kinematic plutons of the Kangguer–Huangshan Shear zone: Inference on the tectonic evolution of the eastern Chinese north Tianshan. American Journal of Science 314, 43-79.

Wang, T., Hong, D.W., Jahn, B.M., Tong, Y., Wang, Y.B., Han, B.F., Wang, X.X., 2006. Timing, petrogenesis, and setting of Paleozoic synorogenic intrusions from the Altai Mountains, Northwest China: implications for the tectonic evolution of an accretionary orogen. The Journal of Geology 114, 735-751.

Wang, T., Jahn, B.-m., Kovach, V.P., Tong, Y., Wilde, S.A., Hong, D.-w., Li, S., Salnikova, E.B., 2014b. Mesozoic intraplate granitic magmatism in the Altai accretionary orogen, NW China: Implications for the orogenic architecture and crustal growth. American Journal of Science 314, 1-42.

Wang, W., Wei, C., Wang, T., Lou, Y., Chu, H., 2009. Confirmation of pelitic granulite in the

Altai orogen and its geological significance. Chinese Science Bulletin 54, 2543-2548.

Wang, W., Wei, C., Zhang, Y., Chu, H., Zhao, Y., Liu, X., 2014c. Age and origin of sillimanite schist from the Chinese Altai metamorphic belt: implications for late Palaeozoic tectonic evolution of the Central Asian Orogenic Belt. International Geology Review 56, 224-236.

Wang, Y., Mooney, W.D., Yuan, X., Coleman, R.G., 2003. The crustal structure from the Altai Mountains to the Altyn Tagh fault, northwest China. Journal of Geophysical Research: Solid Earth 108, 2322.

Wang, Y., Li, J., Sun, G., 2008. Postcollisional Eastward Extrusion and Tectonic Exhumation along the Eastern Tianshan Orogen, Central Asia: Constraints from Dextral Strike-Slip Motion and 40Ar/39ArAr40/Ar39 Geochronological Evidence. The Journal of Geology 116, 599-618.

Wang, Y., Wang, J., Wang, L., Long, L., Tang, P., Liao, Z., Zhang, H., Shi, Y., 2012. The Tuerkubantao ophiolite mélange in Xinjiang, NW China: New evidence for the Erqis suture zone. Geoscience Frontiers 3, 587-602.

Wilhem, C., Windley, B.F., Stampfli, G.M., 2012. The Altaids of Central Asia: A tectonic and evolutionary innovative review. Earth-Science Reviews 113, 303-341.

Windley, B.F., Kröner, A., Guo, J., Qu, G., Li, Y., Zhang, C., 2002. Neoproterozoic to Paleozoic Geology of the Altai Orogen, NW China: New Zircon Age Data and

Tectonic Evolution. The Journal of Geology 110, 719-737.

Windley, B.F., Alexeiev, D., Xiao, W., Kroner, A., Badarch, G., 2007. Tectonic models for accretion of the Central Asian Orogenic Belt. Journal of the Geological Society 164, 31-47.

Xia, X., Sun, M., Geng, H., Sun, Y., Wang, Y., Zhao, G., 2011. Quasi-simultaneous determination of U-Pb and Hf isotope compositions of zircon by excimer laser-ablation multiple-collector ICPMS. Journal of Analytical Atomic Spectrometry 26, 1868-1871.

Xiao, W., Windley, B.F., Hao, J., Zhai, M., 2003. Accretion leading to collision and the Permian Solonker suture, Inner Mongolia, China: Termination of the central Asian orogenic belt. Tectonics 22, 1069.

Xiao, W., Han, C., Yuan, C., Sun, M., Lin, S., Chen, H., Li, Z., Li, J., Sun, S., 2008. Middle Cambrian to Permian subduction-related accretionary orogenesis of Northern Xinjiang, NW China: implications for the tectonic evolution of central Asia. Journal of Asian Earth Sciences 32, 102-117.

Xiao, W., Windley, B., Huang, B., Han, C., Yuan, C., Chen, H., Sun, M., Sun, S., Li, J., 2009a. End-Permian to mid-Triassic termination of the accretionary processes of the southern Altaids: implications for the geodynamic evolution, Phanerozoic continental growth, and metallogeny of Central Asia. International Journal of Earth Sciences 98, 1189-1217.

Xiao, W., Windley, B., Yuan, C., Sun, M., Han, C., Lin, S., Chen, H., Yan, Q., Liu, D., Qin, K., Li, J., Sun, S., 2009b. Paleozoic multiple subduction-accretion processes of the southern Altaids. American Journal of Science 309, 221-270.

Xiao, W., Huang, B., Han, C., Sun, S., Li, J., 2010. A review of the western part of the Altaids: A key to understanding the architecture of accretionary orogens. Gondwana Research 18, 253–273.

Xiao, W., Windley, B.F., Allen, M.B., Han, C., 2013. Paleozoic multiple accretionary and collisional tectonics of the Chinese Tianshan orogenic collage. Gondwana Research 23, 1316-1341.

Xiao, W., Santosh, M., 2014. The western Central Asian Orogenic Belt: A window to accretionary orogenesis and continental growth. Gondwana Research 25, 1429–1444.

Xiao, W., Windley, B., Sun, S., Li, J., Huang, B., Han, C., Yuan, C., Sun, M., Chen, H., 2015. A Tale of Amalgamation of Three Collage Systems in the Permian–Middle Triassic in Central-East Asia: Oroclines, Sutures, and Terminal Accretion. Annual Review of Earth and Planetary Sciences 43, doi: 10.1146/annurev-earth-060614-105254.

Xu, Z., Wang, Q., Pêcher, A., Liang, F., Qi, X., Cai, Z., Li, H., Zeng, L., Cao, H., 2013. Orogen-parallel ductile extension and extrusion of the Greater Himalaya in the late Oligocene and Miocene. Tectonics 32, 191-215.

Yakubchuk, A., 2004. Architecture and mineral deposit settings of the Altaid orogenic collage: a revised model. Journal of Asian Earth Sciences 23, 761-779.

Yan, S., Chen, W., Wang, Y., Zhang, Z., Chen, B., 2004. $^{40}Ar/^{39}Ar$ dating and its significance of the Ertix gold metallogenic belt in the Altay orogen, Xinjiang. Acta Geologica Sinica, 500-506 (in Chinese with the English abstract).

Yang, T., Li, J., Liang, M., Wang, Y., 2015. Early Permian mantle–crust interaction in the south-central Altaids: High-temperature metamorphism, crustal partial melting, and mantle-derived magmatism. Gondwana Research 28, 371-390.

Yuan, C., Sun, M., Xiao, W., Li, X., Chen, H., Lin, S., Xia, X., Long, X., 2007. Accretionary orogenesis of the Chinese Altai: insights from Paleozoic granitoids. Chemical Geology 242, 22-39.

Yuan, W., Carter, A., Dong, J., Bao, Z., An, Y., Guo, Z., 2006. Mesozoic–Tertiary exhumation history of the Altai Mountains, northern Xinjiang, China: New constraints from apatite fission track data. Tectonophysics 412, 183-193.

Zhang, C.L., Santosh, M., Zou, H.B., Xu, Y.G., Zhou, G., Dong, Y.G., Ding, R.F., Wang, H.Y., 2012. Revisiting the "Irtish tectonic belt": Implications for the Paleozoic tectonic evolution of the Altai orogen. Journal of Asian Earth Sciences 52, 117-133.

Zhang, J., Zheng, Y., 1993. A Thrust-wrench Model for the Altay Orogenic Belt. Acta Scicentiarum Naturalum Universitis Pekinesis 29, 745-753 (in Chinese with English abstract).

Zhang, J., Sun, M., Schulmann, K., Zhao, G., Wu, Q., Jiang, Y., Guy, A., Wang, Y., 2015. Distinct deformational history of two contrasting tectonic domains in the Chinese Altai: their significance in understanding accretionary orogenic process. Journal of Structural Geology 73, 64-82.

Zhuang, Y.X., 1994. The pressure-temperature-space-time (PTSt) evolution of metamorphism and development mechanism of the thermal-structural-gneiss domes in the Chinese Altaids. Acta Geologica Sinica 68, 35-47 (In Chinese with the English abstract).

Zonenshain, L.P., Kuzmin, M.I., Natapov, L.M., Page, B.M., 1990. Geology of the USSR: a plate-tectonic synthesis. American Geophysical Union 21, 242. pp

Figure captions

Fig. 1. (a) A simplified tectonic map of the western CAOB after Şengör et al. (1993) and Windley et al. (2007) and Chen et al. (2014). The inset topographic image is from Amante and Eakins (2009). In this paper, we refer the south Mongolia orogenic system (SMOS) to represent the intra-oceanic arc systems in the East Junggar and southern Mongolia (Xiao et al., 2008; Kröner et al., 2010); the Kazakhstan orogenic system (KOS) and the peri-Siberian orogenic system (PSOS) to represent arc systems to the south and north of the Irtysh/Chara shear zones, respectively. Note that major late Paleozoic strike-slip faults were highlighted. ISZ: Irtysh Shear Zone; BF: Bulgan Fault; NEF: North-East Fault; CSZ: Chara Shear Zone; CKF: Central Kazakhstan Fault; NNF: Nikolaiev-Nalati Fault; CANTF: Chingiz-Alakol-North Tian Shan Fault; MTSZ: Main Tianshan Shear Zone. (b) Geological map in the area of the Chinese Altai after Choulet et al. (2012), Li et al. (2014a) and Li et al. (2015b). The time range of granitoids is based on the summary by Tong et al. (2014) and Chen et al. (2010), whereas major faults are based on Qu et al. (1994), Laurent-Charvet et al. (2003), Briggs et al. (2007), Jiang et al. (2015) and Zhang et al. (2015).

Fig. 2. Geological map in the Fuyun area of the southern Chinese Altai based on 1:20 000 geological maps. Note that the map highlights major structural elements and published geochronological data (Laurent-Charvet et al., 2003; Briggs et al., 2007; Li et al., 2014b; Li

et al., 2015b). M1-M4 represents Mylonite Zones 1-4. The red star with white fill shows the observed location by Briggs et al. (2007)

Fig. 3. (a-b) Geological map and transect of the southern domain of the Irtysh Shear Zone. See the location in Fig. 2. (c-h) Stereonet plots (lower hemisphere, equal area) for the mylonitic fabric and stretching lineation of Mylonite Zone 4, S_2 fabric and associated L_2 lineation, as well as the hinge (B_{32}) and axil plane of F_3. S_2 in this area defines a β axis at 11-101 (Fig. 3e), which together with the trace of axial plane of antiform/synform (~105° trending) defines an axial plane of F_3 at 70-015 (Fig. 3h). Note that granitic dykes are displaced by Mylonite Zone 4**.**

Fig. 4. (a-b) Geological map and transect of the southern domain of the Irtysh Shear Zone to the east of Fig. 3. The location is indicated in Fig. 2. (c-h) Stereonet plots (lower hemisphere, equal area) for the mylonitic fabric and stretching lineation of Mylonite Zone 4, S_2 fabric and associated L_2 lineation, and the hinge (B_{32}) and axial plane of F_3. S_2 in this area defines a β axis at 33-114 (Fig. 4e), which together with the trace of axial plane of antiform/synform at 127° constrains an axial plane of F_3 at 69-37 (Fig. 4h).

Fig. 5. (a-b) Geological map and transect of the northern domain of the Irtysh Shear Zone

(see the location in Fig. 2). (c-h) Stereonet plots (lower hemisphere, equal area) for mylonitic fabrics and stretching lineations of Mylonite Zone 1-3, and axial planar fabric and hinge of F_3. Note that granitic dykes cut D_3 shearing fabrics of Mylonite Zones 2-3.

Fig. 6. Photographs of representative structures in the Irtysh Shear Zone**.** (a) Folded S_1 fabric with axial plane parallel to S_2; (b) A S_1 fabric defined by preferred alignment of quartz inclusions within garnet, which shows a high angle with the external S_2 fabric; (c) A L_2 stretching lineation defined by preferred alignment of amphiboles; (d) A L_2 stretching lineation defined by stretching quartz aggregate; (e) Preferred alignment of sillimanite indicating syn-S_2 growth; (f) A quartz rod defining L_3 stretching lineation within Mylonite Zone 3; (g-h) Asymmetric fold and σ-type quartz grains demonstrating sinistral shearing of Mylonite Zones 1 and 2.

Fig. 7. Photographs of representative structures in the Irtysh Shear Zone. (a-c) σ-type quartz and S-C fabric illustrating sinistral shearing of Mylonite Zone 3 and 4; (d) F_3 folds with steeply dipping axial planes in the southern domain of the Irtysh Shear Zone; (e) A asymmetric F_3 fold in the southern domain; (f) L_2 stretching lineations slightly deflected by F_3 folds in the southern domain. (g) Isoclinal F_3 folds in the northern domain; (h) Local occurrence of L_2 stretching lineations within folded S_2 layers in the northern domain.

Fig. 8. Age probability diagrams of zircons from two mica schists of the Irtysh Complex.

Fig. 9. (a) A schematic diagram showing the geometry of the Irtysh Shear Zone. (b-d) Schematic cartoons showing a possible scenario for late Paleozoic tectonic evolution of the Irtysh Shear Zone in response to the convergence between the Chinese Altai and the intraoceanic arc system of the East/West Junggar.

Fig. 10. A simplified reconstruction of the CAOB in the late Paleozoic after Şengör et al. (1993), Natal'in and Şengör (2005) and Xiao et al. (2015). Note that the convergence of the Siberian, Tarim and Baltic cratons is possibly linked with the late Paleozoic development of major strike-slip shear zones and the lateral migration of internal segments within the western CAOB as illustrated in the inset cartoon.

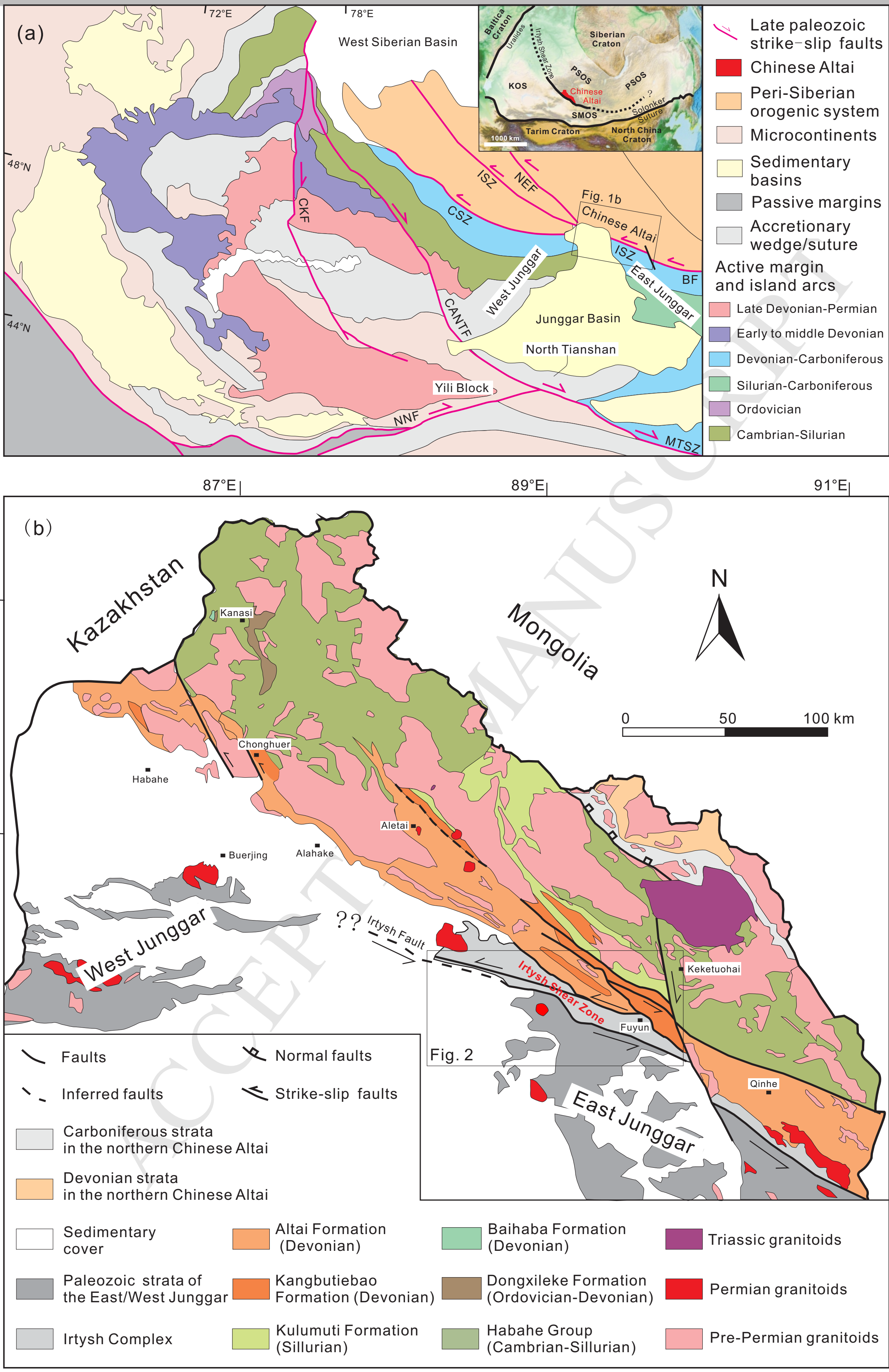
(a)
72°E
78°E
West Siberian Basin
48°N
44°N
Baltica Craton
Uralides
Irtysh Shear Zone
Siberian Craton
PSOS
KOS
Chinese Altai
SMOS
Solonker Suture
Tarim Craton
North China Craton
1000 km
CKF
ISZ
NEF
CSZ
Fig. 1b
Chinese Altai
ISZ
East Junggar
BF
West Junggar
CANTF
Junggar Basin
North Tianshan
Yili Block
NNF
MTSZ
Late paleozoic strike-slip faults
Chinese Altai
Peri-Siberian orogenic system
Microcontinents
Sedimentary basins
Passive margins
Accretionary wedge/suture
Active margin and island arcs
Late Devonian-Permian
Early to middle Devonian
Devonian-Carboniferous
Silurian-Carboniferous
Ordovician
Cambrian-Silurian
87°E
89°E
91°E
48°45′ N
47°45′ N
(b)
Kazakhstan
Mongolia
N
0
50
100 km
Kanasi
Chonghuer
Habahe
Aletai
Buerjing
Alahake
West Junggar
?? Irtysh Fault
Irtysh Shear Zone
Keketuohai
Fuyun
Fig. 2
Qinhe
East Junggar
Faults
Normal faults
Inferred faults
Strike-slip faults
Carboniferous strata in the northern Chinese Altai
Devonian strata in the northern Chinese Altai
Sedimentary cover
Altai Formation (Devonian)
Baihaba Formation (Devonian)
Triassic granitoids
Paleozoic strata of the East/West Junggar
Kangbutiebao Formation (Devonian)
Dongxileke Formation (Ordovician-Devonian)
Permian granitoids
Irtysh Complex
Kulumuti Formation (Sillurian)
Habahe Group (Cambrian-Sillurian)
Pre-Permian granitoids

Fig. 1

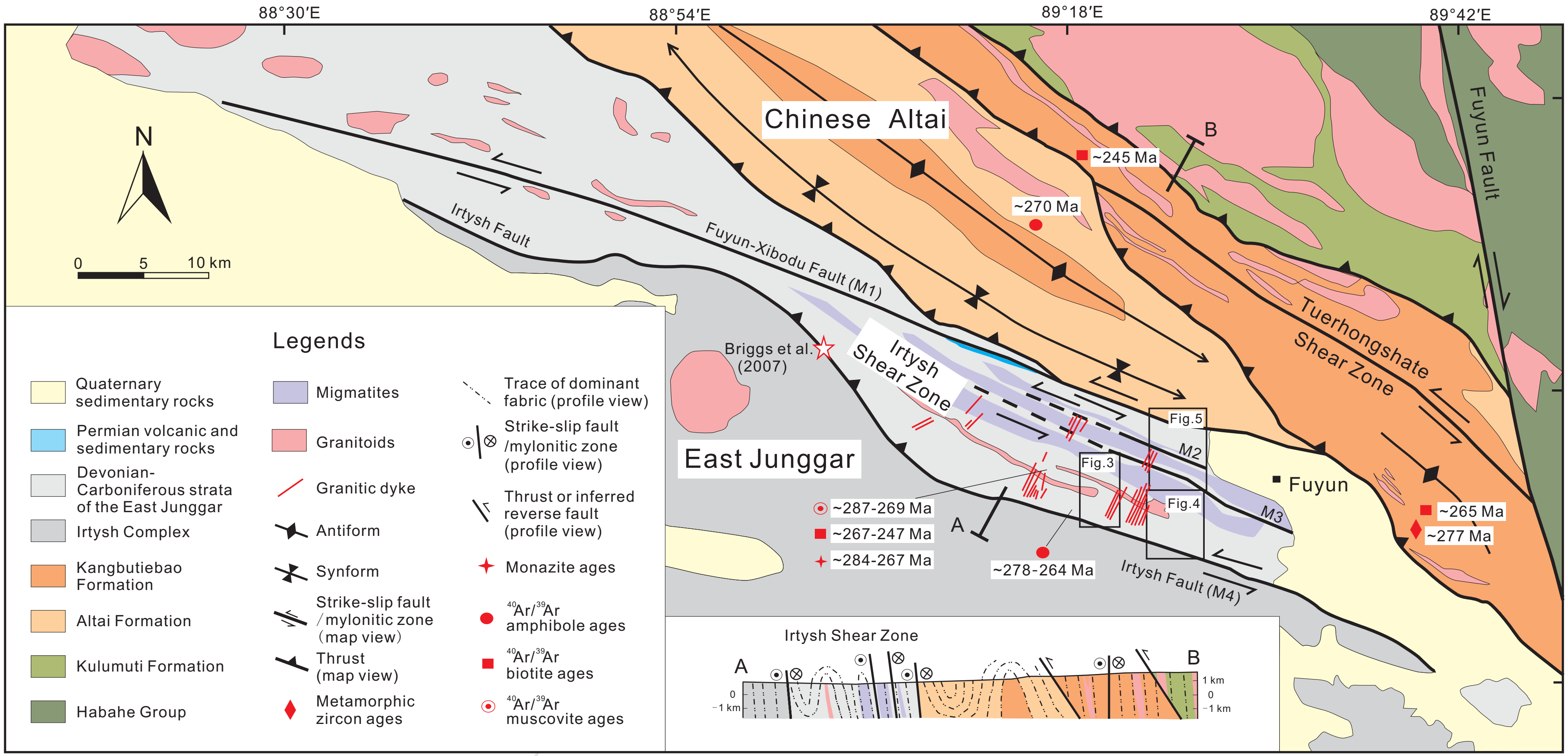
88°30′E
88°54′E
89°18′E
89°42′E
47°15′N
47°03′N
46°51′N
N
0 5 10 km
Chinese Altai
East Junggar
Irtysh Fault
Fuyun-Xibodu Fault (M1)
Irtysh Shear Zone
Tuerhongshate Shear Zone
Fuyun Fault
Irtysh Fault (M4)
M2
M3
Fuyun
Briggs et al. (2007)
~245 Ma
~270 Ma
~265 Ma
~277 Ma
~278-264 Ma
~287-269 Ma
~267-247 Ma
~284-267 Ma
Fig.3
Fig.4
Fig.5
A
B
Legends
Quaternary sedimentary rocks
Permian volcanic and sedimentary rocks
Devonian-Carboniferous strata of the East Junggar
Irtysh Complex
Kangbutiebao Formation
Altai Formation
Kulumuti Formation
Habahe Group
Migmatites
Granitoids
Granitic dyke
Antiform
Synform
Strike-slip fault / mylonitic zone (map view)
Thrust (map view)
Metamorphic zircon ages
Trace of dominant fabric (profile view)
Strike-slip fault /mylonitic zone (profile view)
Thrust or inferred reverse fault (profile view)
Monazite ages
40Ar/39Ar amphibole ages
40Ar/39Ar biotite ages
40Ar/39Ar muscovite ages
Irtysh Shear Zone
1 km
0
−1 km

Fig. 2

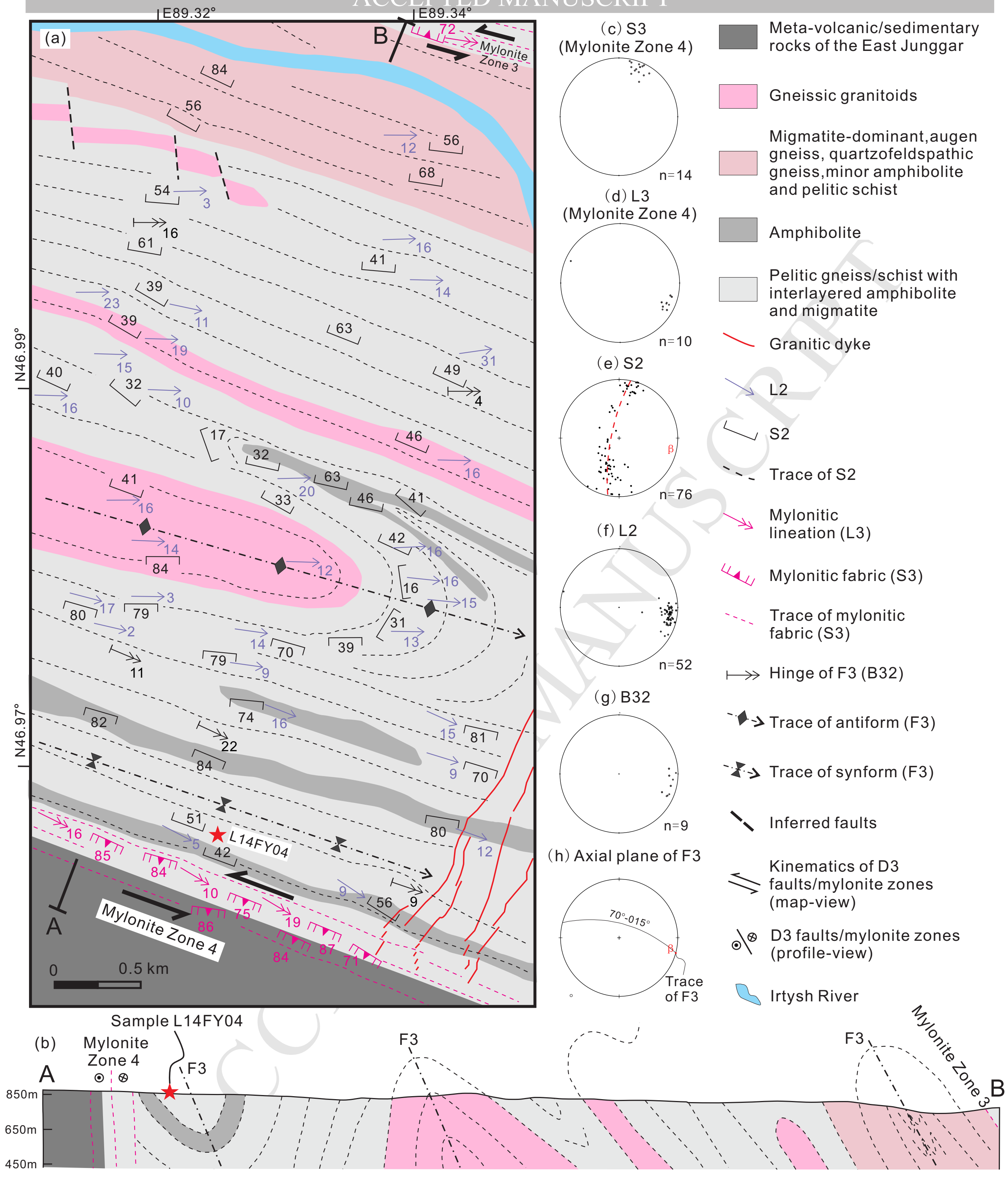

(a)
E89.32°
E89.34°
N46.99°
N46.97°
B
A
Mylonite Zone 3
Mylonite Zone 4
L14FY04
0
0.5 km
(c) S3
(Mylonite Zone 4)
n=14
(d) L3
(Mylonite Zone 4)
n=10
(e) S2
n=76
(f) L2
n=52
(g) B32
n=9
(h) Axial plane of F3
70°-015°
Trace of F3
Meta-volcanic/sedimentary rocks of the East Junggar
Gneissic granitoids
Migmatite-dominant, augen gneiss, quartzofeldspathic gneiss, minor amphibolite and pelitic schist
Amphibolite
Pelitic gneiss/schist with interlayered amphibolite and migmatite
Granitic dyke
L2
S2
Trace of S2
Mylonitic lineation (L3)
Mylonitic fabric (S3)
Trace of mylonitic fabric (S3)
Hinge of F3 (B32)
Trace of antiform (F3)
Trace of synform (F3)
Inferred faults
Kinematics of D3 faults/mylonite zones (map-view)
D3 faults/mylonite zones (profile-view)
Irtysh River
(b)
Sample L14FY04
Mylonite Zone 4
F3
850m
650m
450m

Fig. 3

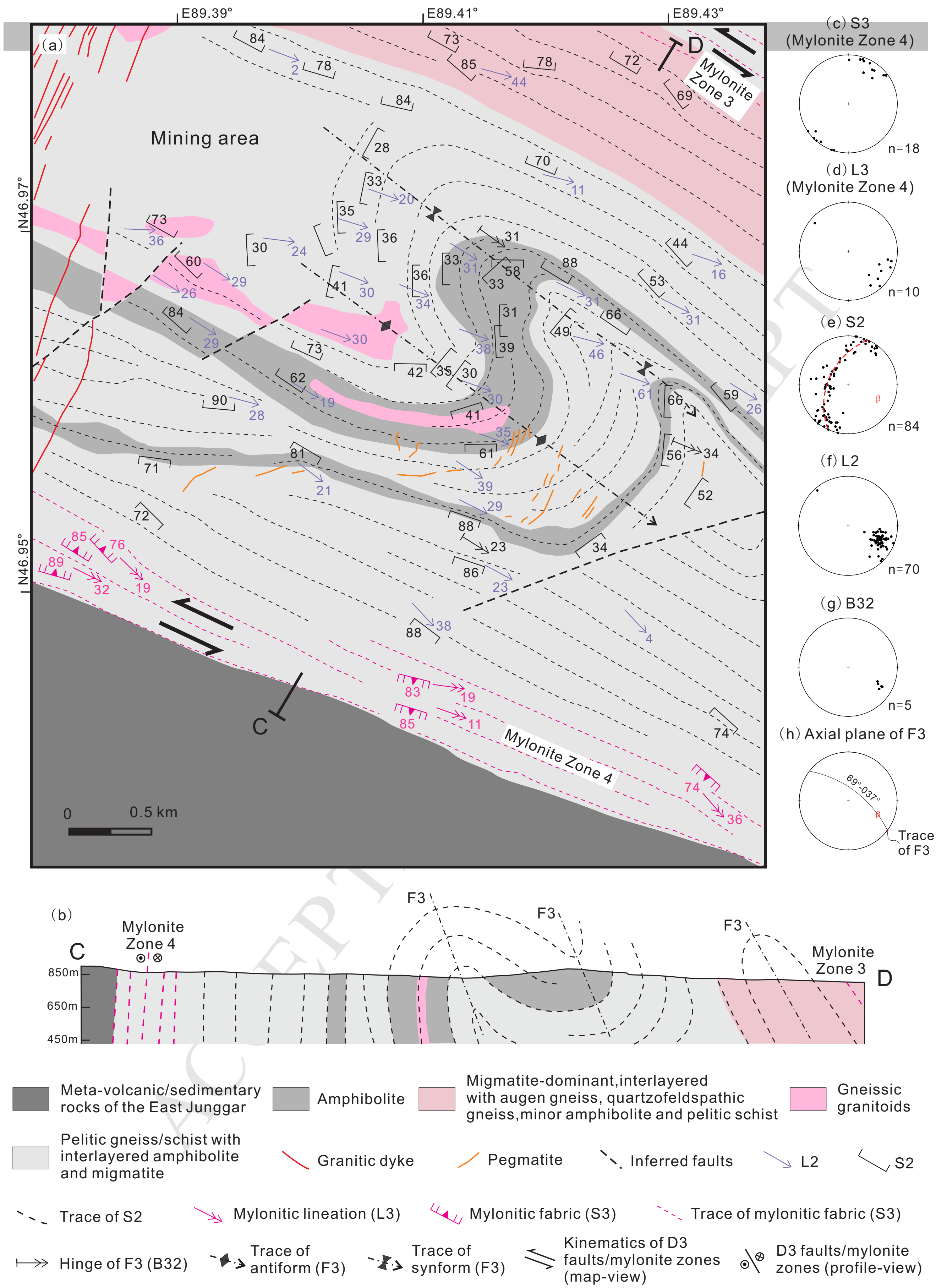

E89.39°
E89.41°
E89.43°
N46.97°
N46.95°
(a)
Mining area
Mylonite Zone 3
Mylonite Zone 4
C
D
0
0.5 km
(c) S3 (Mylonite Zone 4)
n=18
(d) L3 (Mylonite Zone 4)
n=10
(e) S2
n=84
(f) L2
n=70
(g) B32
n=5
(h) Axial plane of F3
69°-037°
Trace of F3
(b)
Mylonite Zone 4
Mylonite Zone 3
F3
850m
650m
450m
Meta-volcanic/sedimentary rocks of the East Junggar
Amphibolite
Migmatite-dominant,interlayered with augen gneiss, quartzofeldspathic gneiss,minor amphibolite and pelitic schist
Gneissic granitoids
Pelitic gneiss/schist with interlayered amphibolite and migmatite
Granitic dyke
Pegmatite
Inferred faults
L2
S2
Trace of S2
Mylonitic lineation (L3)
Mylonitic fabric (S3)
Trace of mylonitic fabric (S3)
Hinge of F3 (B32)
Trace of antiform (F3)
Trace of synform (F3)
Kinematics of D3 faults/mylonite zones (map-view)
D3 faults/mylonite zones (profile-view)

Fig. 4

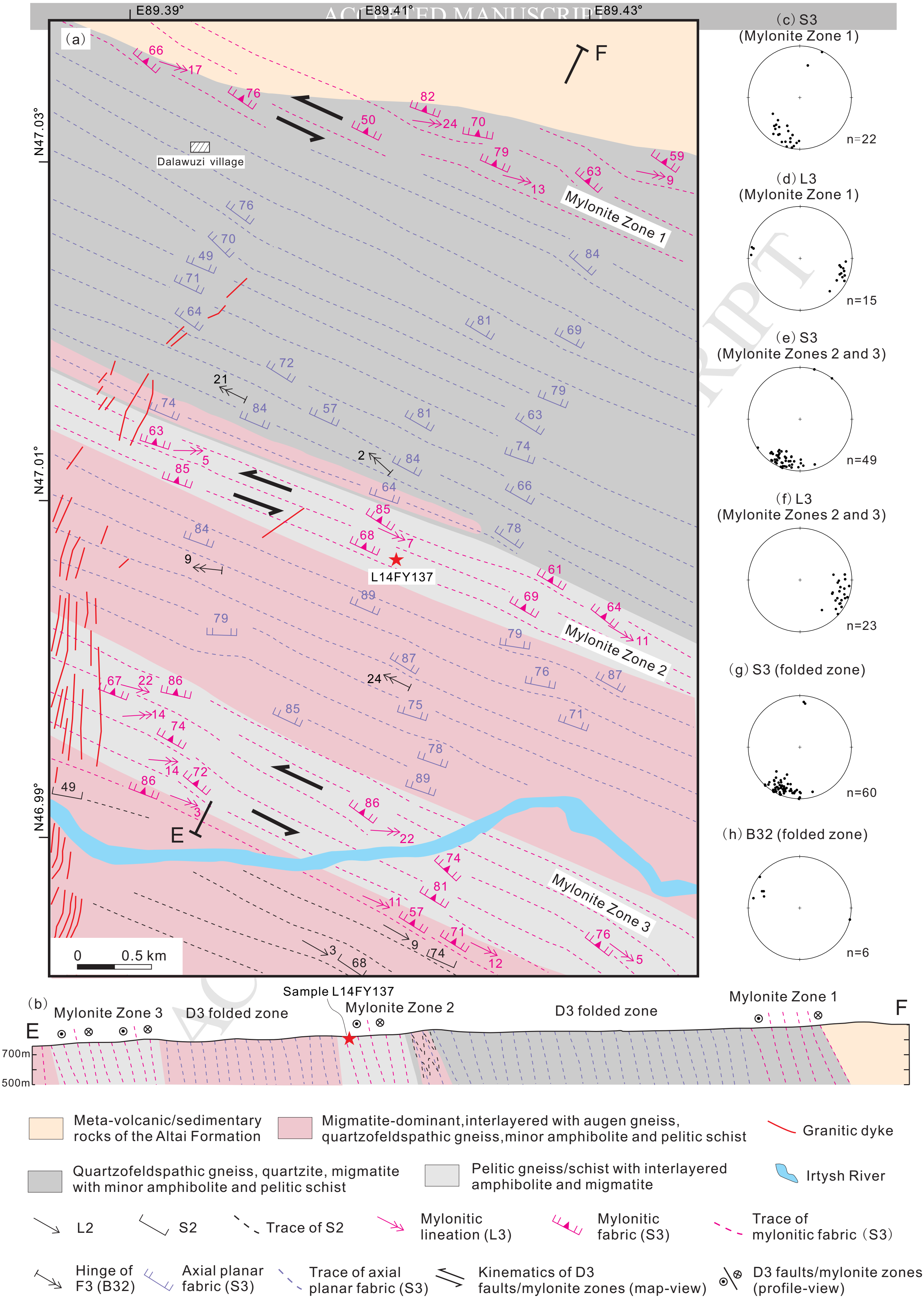

E89.39°
E89.41°
E89.43°
N47.03°
N47.01°
N46.99°
(a)
F
E
Dalawuzi village
Mylonite Zone 1
Mylonite Zone 2
Mylonite Zone 3
L14FY137
0 0.5 km
(c) S3 (Mylonite Zone 1)
n=22
(d) L3 (Mylonite Zone 1)
n=15
(e) S3 (Mylonite Zones 2 and 3)
n=49
(f) L3 (Mylonite Zones 2 and 3)
n=23
(g) S3 (folded zone)
n=60
(h) B32 (folded zone)
n=6
(b)
Sample L14FY137
Mylonite Zone 3
D3 folded zone
Mylonite Zone 2
D3 folded zone
Mylonite Zone 1
700m
500m
Meta-volcanic/sedimentary rocks of the Altai Formation
Migmatite-dominant, interlayered with augen gneiss, quartzofeldspathic gneiss, minor amphibolite and pelitic schist
Granitic dyke
Quartzofeldspathic gneiss, quartzite, migmatite with minor amphibolite and pelitic schist
Pelitic gneiss/schist with interlayered amphibolite and migmatite
Irtysh River
L2
S2
Trace of S2
Mylonitic lineation (L3)
Mylonitic fabric (S3)
Trace of mylonitic fabric (S3)
Hinge of F3 (B32)
Axial planar fabric (S3)
Trace of axial planar fabric (S3)
Kinematics of D3 faults/mylonite zones (map-view)
D3 faults/mylonite zones (profile-view)

Fig. 5

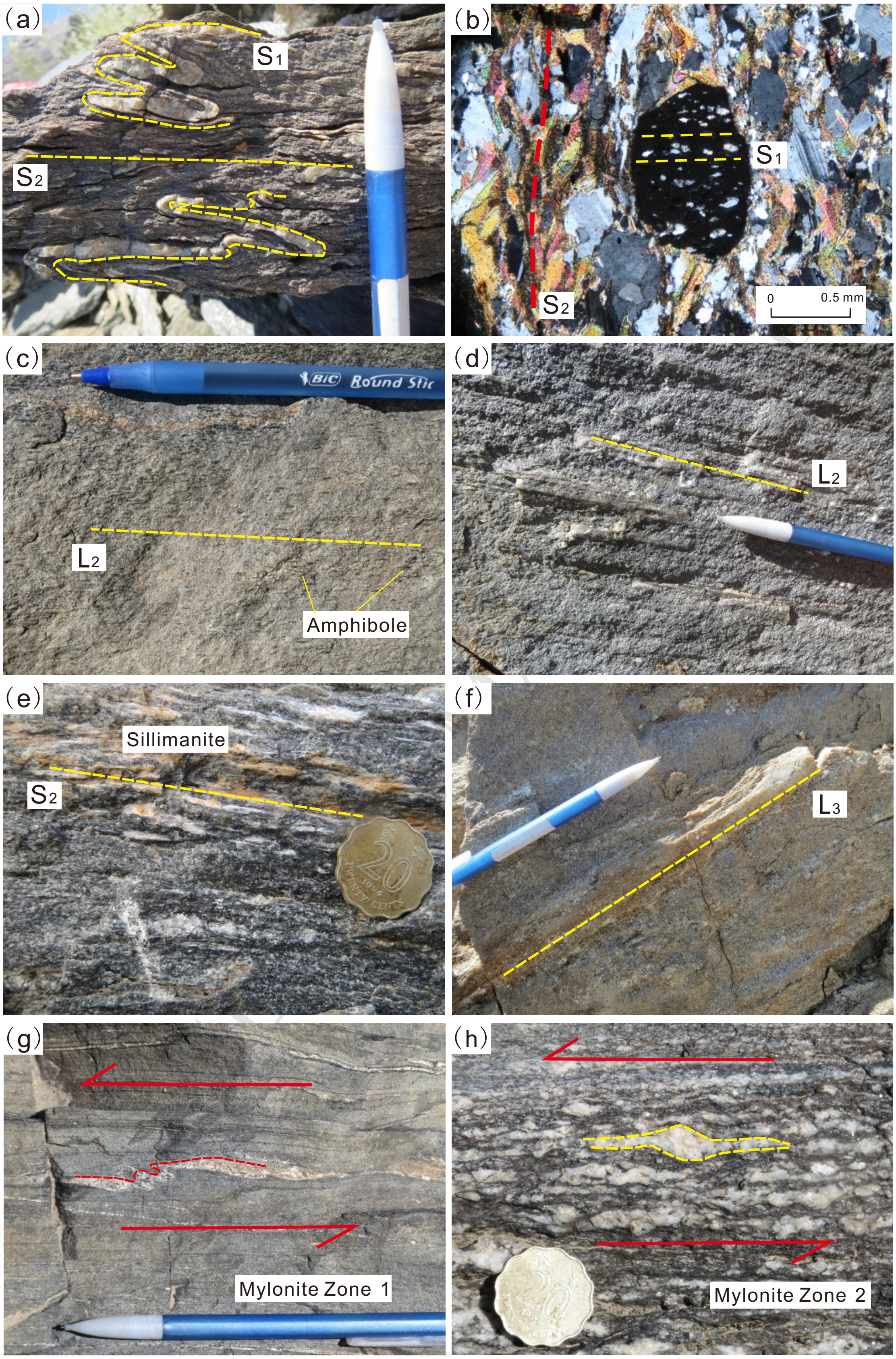
(a)
S1
S2
(b)
S1
S2
0
0.5 mm
(c)
BIC Round Stic
L2
Amphibole
(d)
L2
(e)
Sillimanite
S2
(f)
L3
(g)
Mylonite Zone 1
(h)
Mylonite Zone 2

Fig. 6

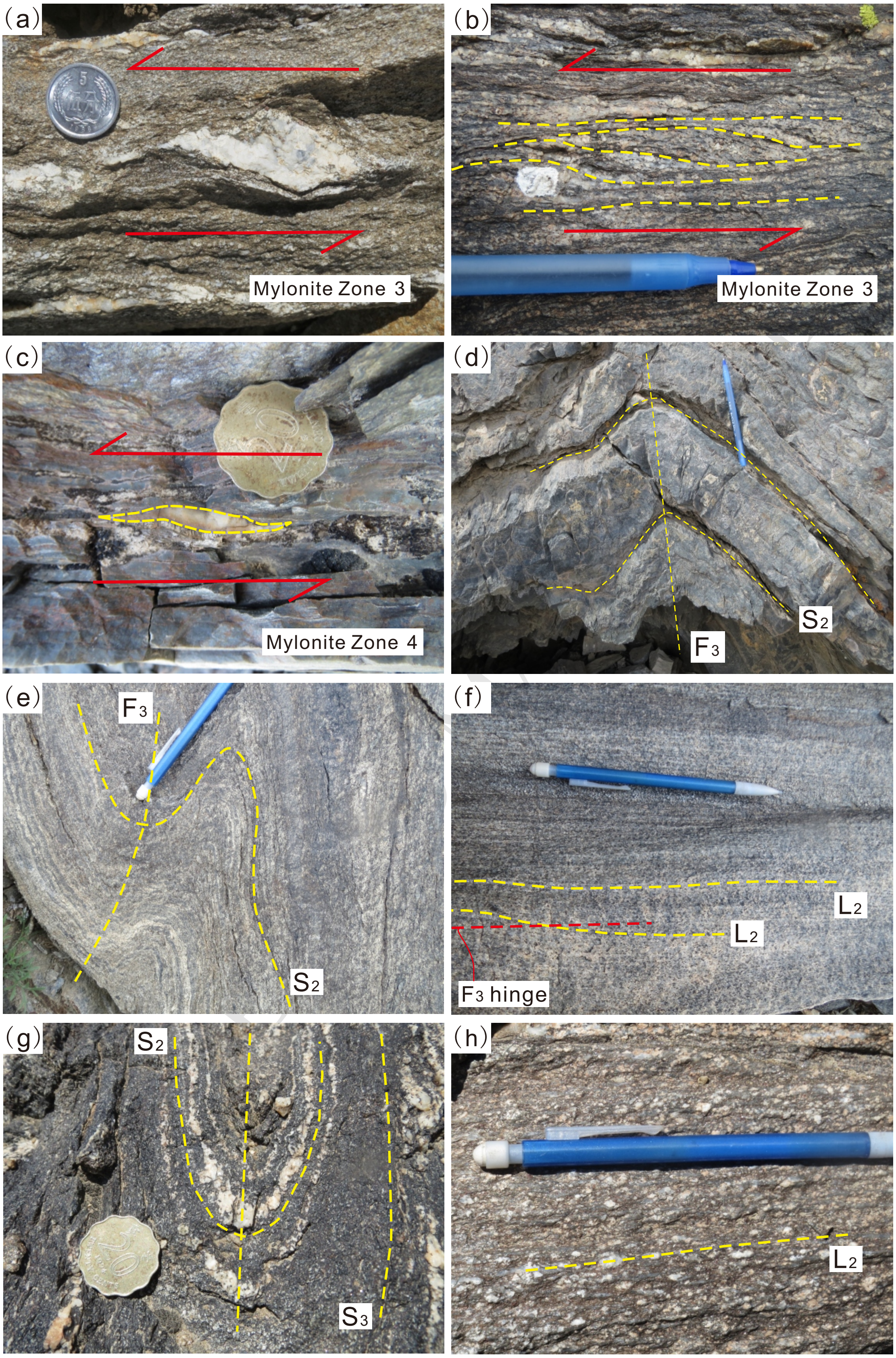
(a)
Mylonite Zone 3
(b)
Mylonite Zone 3
(c)
Mylonite Zone 4
(d)
S2
F3
(e)
F3
S2
(f)
L2
L2
F3 hinge
(g)
S2
S3
(h)
L2

Fig. 7

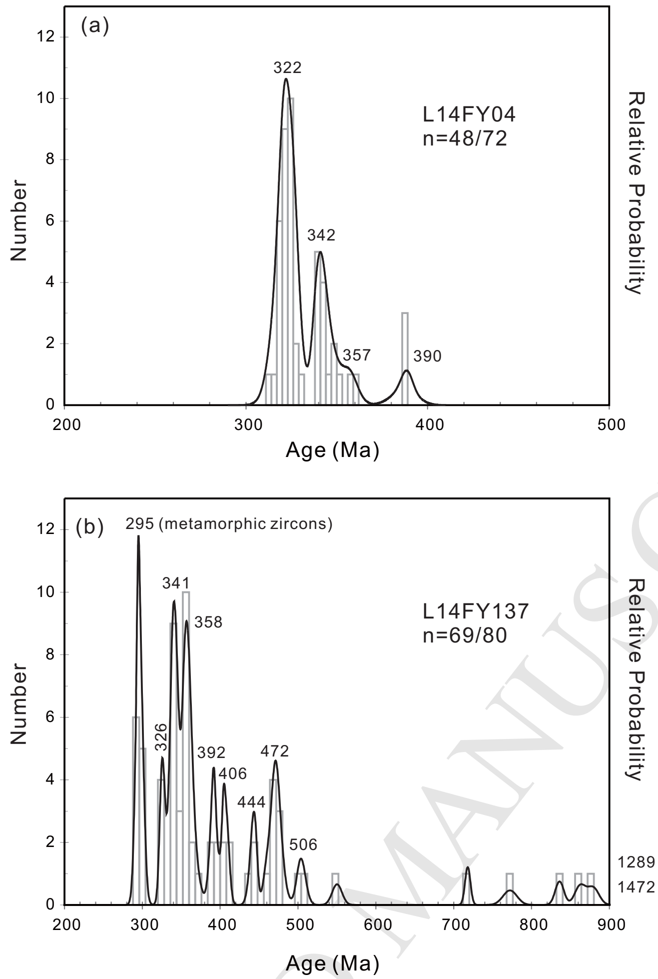
(a)
322
342
357
390
L14FY04
n=48/72
Number
Relative Probability
Age (Ma)
0
2
4
6
8
10
12
200
300
400
500
(b)
295 (metamorphic zircons)
341
358
326
392
406
444
472
506
1289
1472
L14FY137
n=69/80
Number
Relative Probability
Age (Ma)
0
2
4
6
8
10
12
200
300
400
500
600
700
800
900

Fig. 8

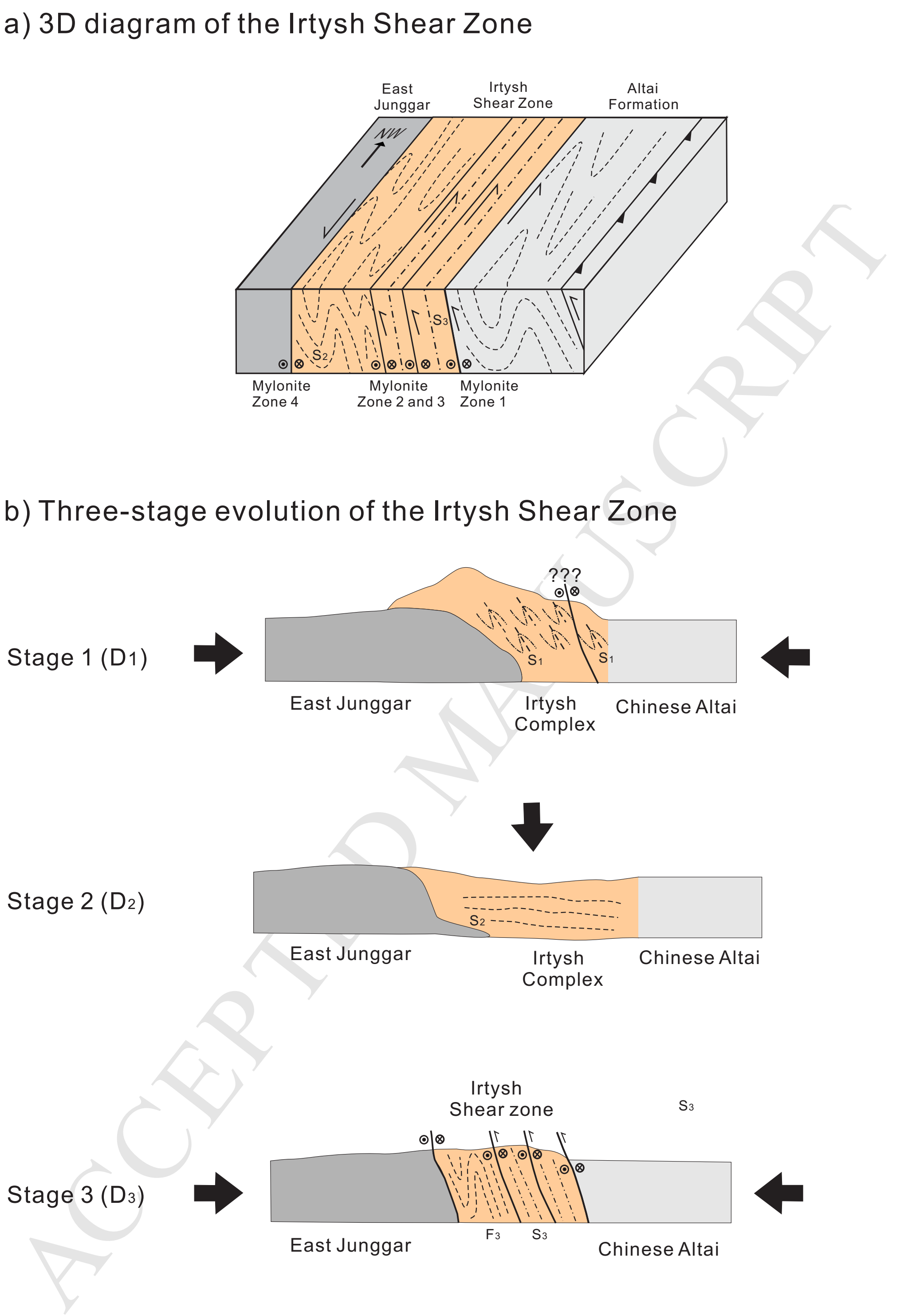
a) 3D diagram of the Irtysh Shear Zone
East Junggar
Irtysh Shear Zone
Altai Formation
NW
S2
S3
Mylonite Zone 4
Mylonite Zone 2 and 3
Mylonite Zone 1
b) Three-stage evolution of the Irtysh Shear Zone
???
Stage 1 (D1)
S1
S1
East Junggar
Irtysh Complex
Chinese Altai
Stage 2 (D2)
S2
East Junggar
Irtysh Complex
Chinese Altai
Irtysh Shear zone
S3
Stage 3 (D3)
East Junggar
F3
S3
Chinese Altai

Fig. 9

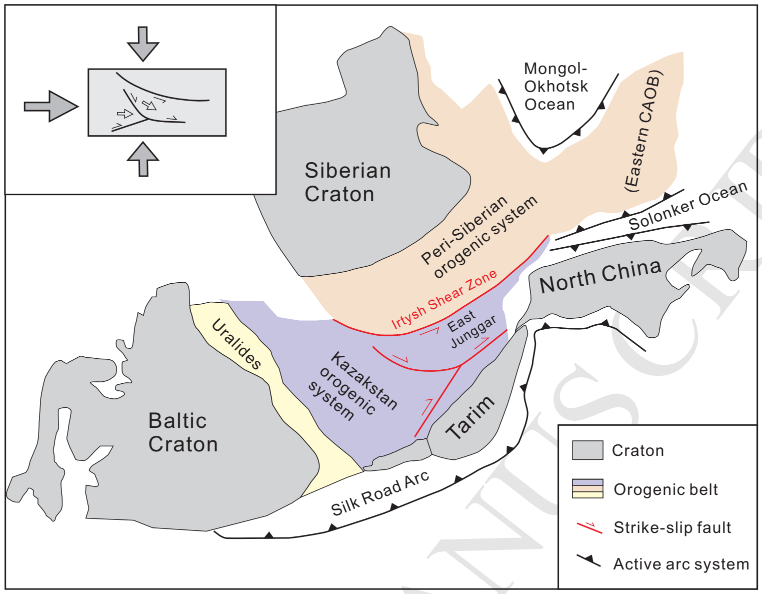
Mongol-
Okhotsk
Ocean
(Eastern CAOB)
Siberian
Craton
Peri-Siberian
orogenic system
Solonker Ocean
North China
Irtysh Shear Zone
East
Junggar
Uralides
Kazakstan
orogenic
system
Baltic
Craton
Tarim
Silk Road Arc
Craton
Orogenic belt
Strike-slip fault
Active arc system

Fig. 10

Research highlights

The Irtysh Shear Zone is a major tectonic boundary in the Central Asia Orogenic Belt;

Three episodes of late Paleozoic deformation (D1-D3) were recognized;

D1-D3 were associated with convergence of arc systems;

D1-D3 represent orogenic thickening, collapse and transpressional deformation;

D3 was possibly reactivated in the Mesozoic to Cenozoic.

Table S1. U–Pb analyses of zricons from the Irtysh Complex. *Excluded from age calculation

	Ratio						Age (Ma)							
Sample #	Pb207/Pb206	1σ	Pb207/U235	1σ	Pb206/U238	1σ	Pb207/Pb 206	1σ	Pb206/U 238	1σ	Pb207/U 235	1σ	Disc%	Th/U
L14FY4_1	0.0533	0.0003	0.4184	0.0054	0.0569	0.0006	339	13	357	4	355	4	−1	0.261
L14FY4_2	0.1144	0.0005	0.7895	0.0048	0.0501	0.0003	1872	7	315	2	591	3	88	0.369
L14FY4_3	0.0586	0.0002	0.3783	0.0031	0.0468	0.0003	554	7	295	2	326	2	11	0.437
L14FY4_4	0.0772	0.0015	0.4415	0.0106	0.0413	0.0003	1126	39	261	2	371	7	42	0.134
L14FY4_5	0.0908	0.0015	0.5697	0.0095	0.0455	0.0003	1443	30	287	2	458	6	60	0.162
L14FY4_6	0.0750	0.0009	0.4596	0.0096	0.0443	0.0004	1133	25	279	2	384	7	38	0.150
L14FY4_7	0.0609	0.0009	0.3790	0.0089	0.0449	0.0004	637	64	283	2	326	7	15	0.152
L14FY4_8	0.0571	0.0002	0.4093	0.0034	0.0520	0.0004	494	9	327	3	348	2	7	0.409
L14FY4_9	0.0566	0.0005	0.3979	0.0042	0.0510	0.0004	476	19	321	2	340	3	6	0.325
L14FY4_10	0.0531	0.0002	0.3741	0.0027	0.0512	0.0004	332	7	322	2	323	2	0	0.500
L14FY4_11	0.0533	0.0002	0.3999	0.0042	0.0544	0.0005	339	7	341	3	342	3	0	0.332
L14FY4_12	0.0549	0.0002	0.4707	0.0044	0.0621	0.0005	409	9	389	3	392	3	1	0.329
L14FY4_13	0.0548	0.0002	0.4074	0.0034	0.0538	0.0004	467	7	338	2	347	2	3	0.412
L14FY4_14	0.0535	0.0005	0.3731	0.0056	0.0505	0.0003	350	20	317	2	322	4	1	0.242
L14FY4_15	0.0530	0.0002	0.4009	0.0040	0.0550	0.0006	328	12	345	4	342	3	−1	0.345
L14FY4_16	0.0797	0.0004	0.4477	0.0056	0.0408	0.0005	1189	5	258	3	376	4	46	0.256
L14FY4_17	0.0554	0.0003	0.3962	0.0052	0.0518	0.0005	428	9	326	3	339	4	4	0.266
L14FY4_18	0.0531	0.0001	0.3989	0.0043	0.0545	0.0006	345	7	342	4	341	3	0	0.320
L14FY4_19	0.0545	0.0003	0.3890	0.0046	0.0517	0.0005	391	8	325	3	334	3	3	0.298
L14FY4_20	0.0743	0.0005	0.4799	0.0049	0.0468	0.0003	1050	14	295	2	398	3	35	0.300
L14FY4_21	0.0578	0.0003	0.4050	0.0042	0.0508	0.0004	524	5	319	2	345	3	8	0.331
L14FY4_22	0.0536	0.0003	0.3765	0.0033	0.0509	0.0003	354	11	320	2	324	2	1	0.406
L14FY4_23	0.0534	0.0001	0.4014	0.0041	0.0546	0.0006	343	6	343	3	343	3	0	0.341
L14FY4_24	0.1040	0.0027	0.5974	0.0072	0.0442	0.0010	1698	48	279	6	476	5	70	0.220
L14FY4_25	0.0636	0.0004	0.4428	0.0081	0.0502	0.0007	728	13	316	4	372	6	18	0.175
L14FY4_26	0.1107	0.0041	0.7382	0.0252	0.0487	0.0004	1811	67	306	2	561	15	83	0.068
L14FY4_27	0.0555	0.0002	0.4147	0.0033	0.0542	0.0004	432	3	340	2	352	2	3	0.424

	Ratio						Age (Ma)							
Sample #	Pb207/Pb206	1σ	Pb207/U235	1σ	Pb206/U238	1σ	Pb207/Pb 206	1σ	Pb206/U 238	1σ	Pb207/U 235	1σ	Disc%	Th/U
L14FY4_28	0.0559	0.0005	0.4026	0.0061	0.0522	0.0006	456	25	328	3	344	4	5	0.226
L14FY4_29	0.1111	0.0057	0.8206	0.0553	0.0508	0.0011	1817	95	320	7	608	31	90	0.032
L14FY4_30	0.0545	0.0002	0.3858	0.0045	0.0513	0.0006	394	40	322	3	331	3	3	0.305
L14FY4_31	0.0689	0.0014	0.4149	0.0085	0.0437	0.0002	896	43	276	1	352	6	28	0.165
L14FY4_32	0.0920	0.0024	0.5674	0.0175	0.0444	0.0004	1533	50	280	2	456	11	63	0.088
L14FY4_33	0.0570	0.0005	0.4007	0.0071	0.0508	0.0005	494	25	319	3	342	5	7	0.195
L14FY4_34	0.0598	0.0009	0.3836	0.0056	0.0466	0.0003	594	31	293	2	330	4	12	0.245
L14FY4_35	0.0543	0.0002	0.4049	0.0033	0.0542	0.0005	383	9	340	3	345	2	1	0.417
L14FY4_36	0.0566	0.0005	0.3955	0.0085	0.0505	0.0007	476	19	317	4	338	6	7	0.161
L14FY4_37	0.0555	0.0003	0.4003	0.0051	0.0524	0.0007	432	11	329	4	342	4	4	0.269
L14FY4_38	0.0558	0.0003	0.3973	0.0025	0.0518	0.0005	443	11	325	3	340	2	4	0.542
L14FY4_39	0.0728	0.0006	0.5657	0.0067	0.0563	0.0005	1009	21	353	3	455	4	29	0.231
L14FY4_40	0.0577	0.0003	0.4578	0.0069	0.0573	0.0007	520	11	359	4	383	5	7	0.208
L14FY4_41	0.0563	0.0006	0.3897	0.0086	0.0497	0.0006	465	22	313	4	334	6	7	0.159
L14FY4_42	0.0982	0.0008	0.8739	0.0232	0.0641	0.0013	1591	15	401	8	638	13	59	0.080
L14FY4_43	0.0750	0.0005	0.5874	0.0107	0.0571	0.0010	1133	12	358	6	469	7	31	0.145
L14FY4_44	0.0533	0.0002	0.4000	0.0044	0.0545	0.0006	339	9	342	3	342	3	0	0.316
L14FY4_45	0.0530	0.0002	0.4067	0.0063	0.0556	0.0009	332	7	349	5	346	5	−1	0.219
L14FY4_46	0.0568	0.0003	0.4029	0.0035	0.0514	0.0004	483	14	323	2	344	3	6	0.392
L14FY4_47	0.0547	0.0004	0.3899	0.0070	0.0514	0.0007	467	15	323	4	334	5	4	0.195
L14FY4_48	0.0539	0.0002	0.4609	0.0073	0.0620	0.0010	369	6	388	6	385	5	−1	0.196
L14FY4_49	0.0535	0.0004	0.3698	0.0051	0.0501	0.0005	350	17	315	3	320	4	1	0.265
L14FY4_50	0.0645	0.0010	0.5474	0.0226	0.0594	0.0015	759	31	372	9	443	15	19	0.067
L14FY4_51	0.0737	0.0018	0.5335	0.0186	0.0512	0.0007	1035	49	322	4	434	12	35	0.081
L14FY4_52	0.0531	0.0002	0.3762	0.0039	0.0513	0.0005	332	6	323	3	324	3	0	0.345
L14FY4_53	0.0585	0.0005	0.4119	0.0074	0.0509	0.0007	550	17	320	4	350	5	9	0.187
L14FY4_54	0.0820	0.0023	0.6129	0.0251	0.0519	0.0008	1256	54	326	5	485	16	49	0.063
L14FY4_55	0.0529	0.0002	0.3775	0.0041	0.0518	0.0006	324	14	325	3	325	3	0	0.329

	Ratio						Age (Ma)							
Sample #	Pb207/Pb206	1σ	Pb207/U235	1σ	Pb206/U238	1σ	Pb207/Pb 206	1σ	Pb206/U 238	1σ	Pb207/U 235	1σ	Disc%	Th/U
L14FY4_56	0.0538	0.0002	0.4108	0.0051	0.0555	0.0007	361	11	348	4	349	4	0	0.275
L14FY4_57	0.0683	0.0006	0.4740	0.0045	0.0505	0.0005	876	17	317	3	394	3	24	0.323
L14FY4_58	0.1667	0.0025	1.3983	0.0282	0.0610	0.0006	2525	25	382	4	888	12	133	0.084
L14FY4_59	0.0546	0.0003	0.3902	0.0051	0.0518	0.0006	398	13	326	4	335	4	3	0.268
L14FY4_60	0.0537	0.0002	0.4148	0.0059	0.0559	0.0008	367	9	351	5	352	4	0	0.235
L14FY4_61	0.0537	0.0002	0.4023	0.0050	0.0543	0.0006	367	9	341	4	343	4	1	0.274
L14FY4_62	0.0529	0.0002	0.3719	0.0034	0.0510	0.0004	324	5	321	2	321	3	0	0.395
L14FY4_63	0.0532	0.0003	0.3795	0.0044	0.0518	0.0006	339	11	325	4	327	3	0	0.310
L14FY4_64	0.0579	0.0004	0.4114	0.0102	0.0512	0.0009	524	15	322	6	350	7	9	0.136
L14FY4_65	0.0533	0.0002	0.3805	0.0044	0.0518	0.0006	343	5	325	4	327	3	1	0.313
L14FY4_66	0.0544	0.0003	0.3849	0.0039	0.0514	0.0005	387	11	323	3	331	3	2	0.350
L14FY4_67	0.0536	0.0002	0.4572	0.0097	0.0618	0.0013	354	6	386	8	382	7	−1	0.149
L14FY4_68	0.0550	0.0004	0.3837	0.0062	0.0505	0.0006	413	17	318	4	330	5	4	0.218
L14FY4_69	0.0535	0.0003	0.3807	0.0049	0.0516	0.0006	350	11	324	4	328	4	1	0.276
L14FY4_70	0.0539	0.0003	0.4007	0.0067	0.0539	0.0008	365	19	338	5	342	5	1	0.206
L14FY4_71	0.0561	0.0003	0.3927	0.0101	0.0504	0.0011	457	11	317	7	336	7	6	0.136
L14FY4_72	0.0729	0.0007	0.4361	0.0041	0.0434	0.0003	1009	19	274	2	367	3	34	0.342
L14FY137_1	0.0526	0.0001	0.3437	0.0044	0.0474	0.0006	309	8	299	4	300	3	0	0.004
L14FY137_2	0.0534	0.0001	0.3446	0.0021	0.0468	0.0002	346	6	295	2	301	2	2	0.009
L14FY137_3	0.0527	0.0001	0.3462	0.0050	0.0477	0.0007	322	6	300	4	302	4	1	0.024
L14FY137_4	0.0539	0.0001	0.3472	0.0047	0.0467	0.0006	365	4	294	4	303	4	3	0.006
L14FY137_5	0.0533	0.0002	0.4201	0.0059	0.0571	0.0008	343	3	358	5	356	4	−1	0.801
L14FY137_6	0.0544	0.0001	0.4229	0.0099	0.0562	0.0013	387	1	353	8	358	7	2	0.103
L14FY137_7	0.0584	0.0001	0.6112	0.0070	0.0760	0.0009	546	4	472	6	484	4	3	0.596
L14FY137_8	0.0566	0.0002	0.6022	0.0084	0.0771	0.0011	476	6	479	6	479	5	0	0.636
L14FY137_9	0.0529	0.0001	0.3795	0.0050	0.0520	0.0007	324	6	327	4	327	4	0	0.128
L14FY137_10	0.0537	0.0003	0.4180	0.0070	0.0565	0.0009	367	11	355	6	355	5	0	0.380
L14FY137_11	0.0561	0.0003	0.4170	0.0050	0.0540	0.0006	454	18	339	4	354	4	4	0.927

	Ratio						Age (Ma)							
Sample #	Pb207/Pb206	1σ	Pb207/U235	1σ	Pb206/U238	1σ	Pb207/Pb 206	1σ	Pb206/U 238	1σ	Pb207/U 235	1σ	Disc%	Th/U
L14FY137_12	0.0541	0.0003	0.5677	0.0061	0.0761	0.0007	372	11	473	4	457	4	−3	0.649
L14FY137_13	0.0566	0.0001	0.5537	0.0041	0.0710	0.0005	476	1	442	3	447	3	1	0.160
L14FY137_14	0.0578	0.0002	0.6456	0.0063	0.0811	0.0008	524	7	502	5	506	4	1	0.473
L14FY137_15	0.0541	0.0003	0.4271	0.0055	0.0573	0.0007	376	15	359	4	361	4	1	0.616
L14FY137_16	0.0665	0.0002	1.1658	0.0138	0.1273	0.0016	822	6	772	9	785	6	2	0.628
L14FY137_17	0.0556	0.0001	0.5738	0.0075	0.0749	0.0010	435	4	466	6	460	5	−1	1.158
L14FY137_18	0.0546	0.0002	0.4462	0.0076	0.0592	0.0010	398	9	371	6	375	5	1	0.650
L14FY137_19	0.0567	0.0002	0.4295	0.0038	0.0549	0.0005	483	6	345	3	363	3	5	0.101
L14FY137_20	0.0570	0.0001	0.5625	0.0038	0.0715	0.0005	500	6	445	3	453	2	2	0.400
L14FY137_21	0.0707	0.0001	1.3945	0.0118	0.1431	0.0012	946	3	862	7	887	5	3	0.534
L14FY137_22	0.0536	0.0001	0.3654	0.0039	0.0495	0.0006	354	6	311	3	316	3	2	0.061
L14FY137_23	0.0555	0.0002	0.4831	0.0068	0.0631	0.0008	432	3	394	5	400	5	1	0.446
L14FY137_24	0.0556	0.0002	0.3852	0.0065	0.0503	0.0009	435	7	316	5	331	5	5	0.019
L14FY137_25	0.0687	0.0001	1.3127	0.0099	0.1385	0.0010	900	4	836	6	851	4	2	0.050
L14FY137_26	0.0536	0.0001	0.3994	0.0062	0.0539	0.0008	367	6	339	5	341	5	1	0.115
L14FY137_27	0.0569	0.0004	0.4049	0.0043	0.0516	0.0004	487	17	325	3	345	3	6	0.312
L14FY137_28	0.0534	0.0001	0.3472	0.0057	0.0471	0.0007	346	6	296	5	303	4	2	0.018
L14FY137_29	0.0561	0.0002	0.4823	0.0037	0.0624	0.0006	457	7	390	4	400	3	2	0.753
L14FY137_30	0.0540	0.0003	0.4200	0.0052	0.0564	0.0006	372	8	354	4	356	4	1	0.585
L14FY137_31	0.0560	0.0001	0.5883	0.0081	0.0762	0.0011	454	1	474	6	470	5	−1	0.609
L14FY137_32	0.0542	0.0002	0.4017	0.0048	0.0538	0.0006	389	7	338	4	343	3	2	0.668
L14FY137_33	0.0537	0.0001	0.3987	0.0048	0.0538	0.0006	367	6	338	4	341	3	1	0.749
L14FY137_34	0.0922	0.0001	3.2944	0.0408	0.2593	0.0033	1472	−30	1486	17	1480	10	0	0.430
L14FY137_35	0.0535	0.0002	0.3509	0.0037	0.0476	0.0005	350	10	300	3	305	3	2	0.010
L14FY137_36	0.0528	0.0001	0.3411	0.0038	0.0468	0.0005	320	6	295	3	298	3	1	0.014
L14FY137_37	0.0562	0.0003	0.4459	0.0069	0.0574	0.0007	457	11	360	4	374	5	4	0.572
L14FY137_38	0.0554	0.0002	0.4739	0.0054	0.0621	0.0007	428	7	388	4	394	4	1	0.726
L14FY137_39	0.0547	0.0001	0.4327	0.0066	0.0573	0.0008	467	6	359	5	365	5	2	0.159

	Ratio						Age (Ma)							
Sample #	Pb207/Pb206	1σ	Pb207/U235	1σ	Pb206/U238	1σ	Pb207/Pb 206	1σ	Pb206/U 238	1σ	Pb207/U 235	1σ	Disc%	Th/U
L14FY137_40	0.0675	0.0016	0.4119	0.0096	0.0444	0.0003	854	51	280	2	350	7	25	0.805
L14FY137_41	0.0692	0.0004	0.5738	0.0047	0.0602	0.0004	906	10	377	3	460	3	22	0.461
L14FY137_42	0.0523	0.0001	0.3381	0.0035	0.0468	0.0005	298	6	295	3	296	3	0	0.008
L14FY137_43	0.0576	0.0001	0.6491	0.0076	0.0817	0.0010	517	-1	506	6	508	5	0	0.474
L14FY137_44	0.0546	0.0001	0.4090	0.0048	0.0543	0.0006	398	38	341	4	348	3	2	0.847
L14FY137_45	0.0534	0.0002	0.3989	0.0050	0.0543	0.0007	346	7	341	4	341	4	0	0.528
L14FY137_46	0.0531	0.0001	0.3985	0.0056	0.0544	0.0007	345	6	341	5	341	4	0	0.255
L14FY137_47	0.0534	0.0001	0.4035	0.0041	0.0548	0.0005	346	6	344	3	344	3	0	0.673
L14FY137_48	0.0538	0.0002	0.4309	0.0056	0.0581	0.0008	361	9	364	5	364	4	0	0.737
L14FY137_49	0.0542	0.0001	0.4278	0.0064	0.0572	0.0009	389	6	359	5	362	5	1	0.290
L14FY137_50	0.0566	0.0002	0.3630	0.0082	0.0463	0.0010	476	5	292	6	314	6	8	0.006
L14FY137_51	0.0531	0.0001	0.3458	0.0041	0.0473	0.0006	332	8	298	4	302	3	1	0.003
L14FY137_52	0.0680	0.0002	1.1054	0.0050	0.1178	0.0006	878	4	718	3	756	2	5	0.525
L14FY137_53	0.0614	0.0001	0.5315	0.0039	0.0627	0.0004	654	4	392	2	433	3	10	0.411
L14FY137_54	0.0599	0.0005	0.3847	0.0082	0.0462	0.0008	598	14	291	5	331	6	14	0.050
L14FY137_55	0.0567	0.0003	0.4041	0.0032	0.0519	0.0005	480	11	326	3	345	2	6	0.654
L14FY137_56	0.0720	0.0008	0.8379	0.0062	0.0849	0.0007	985	24	525	4	618	3	18	0.392
L14FY137_57	0.0535	0.0002	0.3440	0.0047	0.0465	0.0006	350	12	293	3	300	4	2	0.007
L14FY137_58	0.0548	0.0002	0.4840	0.0060	0.0641	0.0008	406	7	400	5	401	4	0	1.075
L14FY137_59	0.0534	0.0002	0.3420	0.0048	0.0464	0.0006	343	3	292	4	299	4	2	0.011
L14FY137_60	0.0532	0.0001	0.3826	0.0046	0.0522	0.0006	345	6	328	4	329	3	0	0.225
L14FY137_61	0.0581	0.0002	0.6066	0.0075	0.0760	0.0011	532	6	472	6	481	5	2	0.511
L14FY137_62	0.0549	0.0002	0.4378	0.0063	0.0578	0.0008	409	-23	362	5	369	4	2	0.769
L14FY137_63	0.0572	0.0001	0.5167	0.0043	0.0654	0.0005	502	4	409	3	423	3	4	0.525
L14FY137_64	0.0564	0.0001	0.5751	0.0061	0.0740	0.0008	478	4	460	5	461	4	0	0.351
L14FY137_65	0.0565	0.0003	0.4203	0.0027	0.0541	0.0005	472	11	340	3	356	2	5	1.120
L14FY137_66	0.0538	0.0002	0.4216	0.0053	0.0569	0.0007	361	7	357	4	357	4	0	0.373
L14FY137_67	0.0548	0.0001	0.3739	0.0024	0.0495	0.0003	467	4	311	2	323	2	4	0.220

	Ratio						Age (Ma)							
Sample #	Pb207/Pb206	1σ	Pb207/U235	1σ	Pb206/U238	1σ	Pb207/Pb 206	1σ	Pb206/U 238	1σ	Pb207/U 235	1σ	Disc%	Th/U
L14FY137_68	0.0580	0.0001	0.7123	0.0087	0.0891	0.0011	528	4	550	6	546	5	−1	0.524
L14FY137_69	0.0536	0.0002	0.4095	0.0056	0.0554	0.0007	354	9	347	4	349	4	0	0.166
L14FY137_70	0.0569	0.0002	0.5083	0.0031	0.0647	0.0004	487	6	404	2	417	2	3	0.695
L14FY137_71	0.0690	0.0001	1.3888	0.0119	0.1461	0.0013	898	4	879	8	884	5	1	0.265
L14FY137_72	0.0838	0.0001	2.6643	0.0392	0.2304	0.0034	1289	6	1336	18	1319	11	−1	0.374
L14FY137_73	0.0696	0.0004	0.5600	0.0056	0.0587	0.0007	917	13	368	4	452	4	23	0.302
L14FY137_74	0.0628	0.0001	0.6100	0.0055	0.0706	0.0007	702	4	440	4	484	3	10	0.234
L14FY137_75	0.0540	0.0001	0.4208	0.0039	0.0565	0.0006	372	2	355	3	357	3	1	0.541
L14FY137_76	0.0544	0.0002	0.4194	0.0067	0.0558	0.0009	387	3	350	5	356	5	2	0.312
L14FY137_77	0.0616	0.0002	0.5558	0.0061	0.0654	0.0007	657	42	408	4	449	4	10	0.303
L14FY137_78	0.0603	0.0002	0.6265	0.0045	0.0755	0.0007	617	14	469	4	494	3	5	0.487
L14FY137_79	0.0815	0.0018	0.6839	0.0173	0.0610	0.0007	1235	43	382	4	529	10	39	1.363
L14FY137_80	0.0701	0.0007	0.4322	0.0046	0.0447	0.0002	931	20	282	1	365	3	29	1.136

comments
Discordance*
Discordance*
Discordance*
Discordance*
Discordance*
Discordance*
Discordance*
Discordance*
Discordance*
Discordance*
Discordance*

comments
Discordance*
Discordance*
Discordance*
Discordance*
Discordance*
Discordance*
Discordance*
Discordance*
Discordance*
Discordance*

comments
Discordance*
Discordance*
Discordance*
Rim
Rim
Rim
Rim
core
core
core
core
core
core
core

comments
core
core
core
core
core
core
core
core
core
core
Rim mixed with core*
core
Rim mixed with core*
core
core
core
Rim
core
core
core
core
core
core
Rim
Rim
core
core
core

comments
Discordance*
Discordance*
Rim
core
core
core
core
core
core
core
Rim*
Rim
core
core
Discordance*
core
Discordance*
Rim
core
Rim
core
core
core
core
core
core
core
Rim mixed with core*

comments
core
core
core
core
core
Discordance*
core
core
core
core
core
Discordance*
Discordance*

Fig. S1. Cathodoluminescence images (CL) of selected zircon crystals.
Circles indicate locations of U-Pb analyses, and black lines represent a scale of 75 μm.

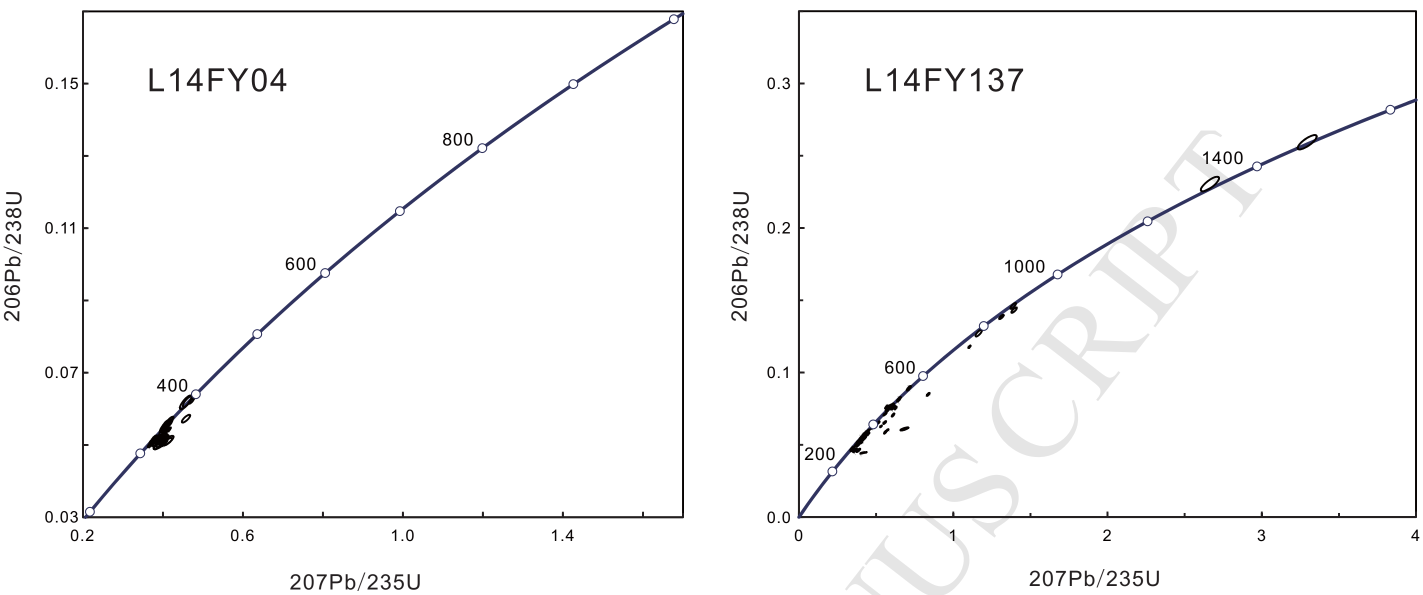

Fig. 2S. Concordia diagrams for zircon U–Pb analyses